This is the peer-reviewed, final accepted version for American Mineralogist, published by the Mineralogical Society of America.
The published version is subject to change. Cite as Authors (Year) Title. American Mineralogist, in press.
DOI: https://doi.org/10.2138/am-2022-8311. http://www.minsocam.org/

Atomic-scale characterization of the oxidation state of Ti in meteoritic hibonite: Implications for early solar system thermodynamics

Revision 2

Word count: 14004

Pierre-Marie Zanetta[1], Venkateswara Rao Manga[1,2], Yao-Jen Chang[1], Tarunika Ramprasad[2], Juliane Weber[1,*], John R. Beckett[3], Thomas J. Zega[1,2]

1. Lunar and Planetary Laboratory, The University of Arizona, Tucson, AZ 85721, U.S.A.; 2. Materials Science and Engineering, The University of Arizona, Tucson, AZ 85721, USA.; 3. Division of Geological and Planetary Sciences, California Institute of Technology, Pasadena, CA 91125, U.S.A *Current address: Chemical Sciences Division, Oak Ridge National Laboratory, Oak Ridge TN 37830, U.S.A.

ABSTRACT

Calcium-aluminum-rich inclusions (CAIs) in chondritic meteorites are composed of refractory minerals thought to be the first solids to have formed in the solar nebula. Among them, hibonite, nominally $CaAl_{12}O_{19}$, holds particular interest because it can incorporate significant amounts of Ti into its crystal structure in both Ti^{3+} and Ti^{4+} oxidation states. The relative amounts of these cations that are incorporated reflect the redox conditions under which the grain formed or last equilibrated and their measurement can provide insight into the thermodynamic landscape of the early solar nebula. Here we develop a new method for the quantification of Ti oxidation states using electron energy-loss spectroscopy (EELS) in an aberration-corrected scanning transmission electron microscope (STEM) in order to apply it to hibonite.

This is the peer-reviewed, final accepted version for American Mineralogist, published by the Mineralogical Society of America.
The published version is subject to change. Cite as Authors (Year) Title. American Mineralogist, in press.
DOI: https://doi.org/10.2138/am-2022-8311. http://www.minsocam.org/

Using a series of Ti-bearing oxides, we find that the onset intensity of the Ti $L_{2,3}$ edge decreases as a function of increasing Ti-oxidation state, which is corroborated by simulated Ti-oxide spectra using first-principles density-functional theory. We test the relationship on a set of synthetic hibonite grains with known $Ti^{4+}/\Sigma Ti$ values and apply the developed method on a hibonite grain from a compact type A inclusion in the Northwest Africa (NWA) 5028 CR2 carbonaceous chondrite. The STEM-EELS data show that the chondritic hibonite grain is zoned with a $Ti^{4+}/\Sigma Ti$ ratio ranging from 0.78±0.04 to 0.93±0.04 over a scale of 100 nm between the core and edge of the grain, respectively. The Ti substitution sites are characterized by experimental and calculated high-angle annular-dark-field (HAADF) images and atomic-level EEL spectrum imaging. Simulated HAADF images reveal that Ti is distributed between the M2 and M4 sites while Mg sits on the M3 site. Quantitative energy-dispersive X-ray spectroscopy shows that this grain is also zoned in Al and Ti. The Mg distribution is not well-correlated with that of Ti and $Ti^{4+}/\Sigma Ti$ at the nanoscale.

The spatial decoupling of the element composition and Ti-oxidation states suggests a multistage evolution for this hibonite grain. We hypothesize that Ti and Mg were incorporated into the structure during condensation at high temperature through multiple reactions. Transient heating, presumably in the solar nebula, adds complexity to the crystal chemistry and potentially redistributed Ti and Mg. Concurrently, the formation of oxygen vacancies as a result of a reducing gas, led to the reduction of Ti^{4+} to Ti^{3+}. The multiple defect reactions occurring in this single hibonite crystal preclude a simple relationship between the $Ti^{4+}/\Sigma Ti$ and the fO_2 of formation. However, moving forward, these measurements are fundamental input for modeling of the thermodynamic conditions under which hibonite formed in the early solar nebula.

Keywords: hibonite, Ti oxidation state, STEM-EELS, chondrites, CAIs, thermodynamic, early solar system, atomic scale, DFT calculations.

This is the peer-reviewed, final accepted version for American Mineralogist, published by the Mineralogical Society of America.
The published version is subject to change. Cite as Authors (Year) Title. American Mineralogist, in press.
DOI: https://doi.org/10.2138/am-2022-8311. http://www.minsocam.org/

INTRODUCTION

The sun and planets formed out of a rotating disk of gas and dust over four billion years ago. It was hypothesized that the temperature of the inner solar nebula was high enough such that solid materials experienced melting, evaporation, and condensation (Cameron 1962). Thermodynamic models subsequently predicted that as the solar gas cooled, solid materials condensed out of it according to their volatility, with the most refractory phases forming at the highest temperatures (Lord 1965; Larimer 1967; Grossman 1972; Lewis 1974; Yoneda and Grossman 1995; Ebel and Grossman 2000; Lodders 2003; Ebel 2006; Grossman et al. 2008; Scott and Krot 2014; Zega et al. 2021). Evidence for such condensation is provided by the mineral assemblages found in Ca-Al-rich inclusions (CAIs) within primitive chondrites. With radiometric age dates of 4.5673 ± 0.00016 billion years (Amelin et al. 2009; Connelly et al. 2012), CAIs mark time zero for our solar system, and our chronological understanding of its evolution is anchored to that time stamp.

Common CAI phases include melilite, spinel, perovskite, hibonite, Ca-pyroxene and forsterite usually with lesser amounts of grossite, metal, and corundum (MacPherson 2014). The composition and structure of these CAI phases are key to determining the chemical pathways through which they formed and to quantifying the conditions under which they condensed or were subsequently altered, whether in the solar nebula or on chondrite parent bodies (Beckett et al. 1988; Simon et al. 1991, 1997; Keller and Buseck 1994; Connolly and Burnett 2003; Grossman et al. 2008; Chi et al. 2009). Thus, measurement of CAI phases from the bulk scale down to the atomic level allows us to gain insight into the thermodynamic landscape surrounding their origins.

Hibonite (nominally $CaAl_{12}O_{19}$) is among the first few phases predicted to form, at temperatures between 1400 and 1900 K, in thermodynamic models that consider a cooling gas of solar composition (e.g., Yoneda and Grossman 1995; Ebel and Grossman 2000; Lodders 2003; Zega et al. 2021). Hibonite

This is the peer-reviewed, final accepted version for American Mineralogist, published by the Mineralogical Society of America.
The published version is subject to change. Cite as Authors (Year) Title. American Mineralogist, in press.
DOI: https://doi.org/10.2138/am-2022-8311. http://www.minsocam.org/

can incorporate a variety of solutes into its crystal structure, including: Mg^{2+}, Zn^{2+}, Fe^{2+} and Fe^{3+}, V^{3+} and V^{4+}, Ti^{3+} and Ti^{4+}, Si^{4+} and Th^{4+} as minor and trace elements (Allen et al. 1978; Beckett et al. 1988; Bermanec et al. 1996; Rakotondrazafy et al. 1996; Simon et al. 1997). Titanium is particularly important because it is often found in significant concentrations in meteoritic hibonite (>0.1 cations per formula unit (Brearley and Jones 1998) and it can occur in multiple oxidation states, thereby providing a redox sensor of nebular conditions (Allen et al. 1978; Armstrong et al. 1982; Beckett et al. 1988; Doyle et al. 2014; Ardit et al. 2016). Quantitative measurement of the Ti oxidation state in hibonite can, therefore, provide fundamental information on the thermodynamic conditions under which it formed or last equilibrated, e.g., composition of the gas, temperature of condensation or thermal processing, and oxygen fugacity (fO_2) (Beckett et al. 1988).

Hibonite is part of the magnetoplumbite group of minerals. It has a space group symmetry of $P6_3/mmc$ and is characterized by unit cell parameters a ≈ 5.5Å, c ≈ 22.0Å (Curien et al. 1956; Bermanec et al. 1996; Nagashima et al. 2010; Holtstam and Hålenius 2020). This structure contains six cation sites and five oxygen sites. Ca occupies a 12-coordinated polyhedron, whereas the aluminum is distributed among five crystallographic sites (named hereafter M1 to M5). M1, M4, and M5 are octahedra, M3 is a tetrahedron, M2 is a trigonal bipyramid, and the atoms within these sites form polyhedral layers perpendicular to the c axis of the hexagonal cell. Atomic substitutions occur abundantly in the hibonite structure, and so the detailed crystal chemistry becomes fundamental to inferring precisely the thermodynamic conditions of the nebular gas at its origin. However, the reactions leading to the Ti incorporation, oxidation, and the location of the substitution in the structure are still debated. Ti can be incorporated into the hibonite structure mainly through two pathways. Ti^{3+} can substitute directly for Al^{3+}, or Ti^{4+} and Mg^{2+} can couple substitute for two Al^{3+} (Allen et al. 1978; Bermanec et al. 1996; Nagashima et al. 2010; Doyle et al. 2014; Berry et al. 2017). The oxidation state of Ti can be further affected by the presence of O vacancies and cation defects, both of

which are expected to occur in the structure (Beckett et al. 1988; Asaduzzaman et al. 2021). Regarding the location of the Ti substitution within the M sites (Al), Beckett et al. (1988) proposed that Ti^{3+} occupies the M2 site while Ti^{4+} occupies the M4 site. More recently, Doyle et al. (2014, 2016) proposed that Ti^{3+} does not occupy the M2 site, but instead occupies the M4 octahedral site, and Ti^{4+} partitions between the M2 trigonal bipyramidal and the M4 octahedral sites. The Mg, when balancing the charge of the Ti, is expected to occupy the M3 site. Oxygen vacancies can also occur and modify the Mg and Ti partitioning (Beckett et al. 1988). The distribution of Ti within the M2 and M4 sites was recently observed by coupling STEM-HAADF and energy dispersive spectroscopy (EDS) measurements (Han et al. 2021). However, the $Ti^{4+}/\Sigma Ti$ distribution over these sites has not yet been investigated by direct measurement. Thus, establishing a clear connection between the cation site occupancy and the oxidation state of Ti in hibonite is crucial to understanding the nature of the substitution reactions, their thermodynamic history, and what they tell us about the thermodynamic landscape of the solar nebula.

Here, we examine the oxidation state of Ti and the chemistry of hibonite via EDS and EELS in an aberration-corrected scanning transmission electron microscope. We: (1) report an alternative method for the quantification of Ti-oxidation state in Ti-bearing oxides using EELS; (2) examine the $Ti^{4+}/\Sigma Ti$ variations in meteoritic hibonite down to the atomic scale; (3) provide new information on the Ti site substitution; and (4) link the $Ti^{4+}/\Sigma Ti$ variation as well as chemical zonation to the thermodynamic history of a hibonite grain from the Northwest Africa (NWA) 5028 CR2 chondrite. We propose that the approach used here is an important steppingstone for the analysis of other Ti-bearing oxides in primitive planetary materials and rigorous treatment of the kinds of defect reactions recorded by them.

SAMPLES AND METHODS

EELS has been used for decades to obtain information on oxidation states of *3d* metals in a wide range of earth, planetary, and synthetic materials from micro to atomic scales (Leapman et al., 1982; Brydson et al., 1993; Garvie et al., 1994; Van Aken et al., 1998; Garvie and Buseck, 1998; Van Aken and Liebscher, 2002; Zega et al., 2003; Muller et al., 2008; Chi et al., 2009; Shao et al., 2010; Tan et al., 2011; 2012). Fitting of linear mixing models on energy-loss near-edge structure (ELNES) is one such approach but requires standards whose valence states, coordination polyhedra, and crystal fields ideally match those of the unknown (e.g., Garvie and Buseck, 1998a; Zega et al., 2003). In comparison, the white-line method, so called because the absorption edges of EELS spectra were first observed on photographic film as white lines (Azaroff and Pease 1974), monitors the chemical shift of EELS spectra to higher energy loss with increasing oxidation state using integration windows (Leapman et al. 1982; Garvie et al. 1994; Garvie and Buseck 1998; Van Aken et al. 1998; Van Aken and Liebscher 2002; Stoyanov et al. 2007). The advantage of the white-line method is that it can accommodate materials with varied crystal chemistry (electrical properties, orientation, site symmetry, etc.) without the need to synthesize endmembers (with systematically varied $Ti^{4+}/\Sigma Ti$ ratios) as is the case with a method based on curve fitting. Previous workers developed a calibration curve for Ti based on the white-line approach (Stoyanov et al. 2007). Thus, our purpose here is to modify it as needed to reflect our laboratory and electron-optical conditions.

Samples

To reproduce the white-line ratio method, we acquired seven high-purity (>99.8%) standards with known amounts of Ti^{4+} and Ti^{3+}. These materials and their Ti-oxidation states include: TiO (Ti^{2+}), Ti_2O_3 (Ti^{3+}), Ti_3O_5 (Ti^{4+}:Ti^{3+}= 1:2), Ti_4O_7 (Ti^{4+}:Ti^{3+}= 1:1), TiO_2 (Ti^{4+}), $FeTiO_3$ (Ti^{4+}), $CaTiO_3$ (Ti^{4+}). All were acquired from commercial suppliers (CERAC, Alfa Asear, Phelly Materials, and SigmaAldrich) in powder form except Ti_4O_7, which was kindly provided by Dr. Lindsay Keller (Keller 1995). Standards were crushed in

144 an agate stone mortar and pestle in dry conditions and deposited onto lacey-carbon films supported
145 by Cu-mesh TEM grids (Fig. S1a). The dry conditions avoided the use of solvents and hence possible
146 alteration of the samples but some grain clustering (up to 200 nm) occurred during the sprinkling of
147 the particles. We measured only those particles that are monodisperse and electron transparent (< 50
148 nm in thickness, see Fig. S1).

149 We also examined synthetic hibonites equilibrated under conditions of controlled temperature
150 and oxygen fugacity (fO_2). We measured the 'ALL' samples reported in Ihinger and Stolper (1986) and
151 Beckett et al. (1988) because their composition and Ti oxidation states are comparable to meteoritic
152 samples. The compositions of these synthetic hibonite samples correspond to the average
153 composition of hibonite in the CG-11 inclusion in the Allende CV3 chondrite. They were chosen
154 because they contain significantly lower concentration of V (which can occur as V^{4+} and V^{3+}) and a
155 higher Ti concentration than the Blue Angel (BA) inclusion from the Murchison meteorite (0.39 vs 1.1
156 V_2O_3 wt.% and 7.3 vs 4.1 TiO2 wt%, respectively; see Armstrong et al. (1982).

157 The $Ti^{4+}/\Sigma Ti$ of these samples was originally measured by electron spin resonance (ESR)
158 spectroscopy (Beckett et al. 1988). We selected the extreme and an intermediate samples of the
159 series that correspond to $Ti^{4+}/\Sigma Ti$ of 0.85±0.01, 0.91±0.01, and 0.95±0.01 for ALL 2-55, ALL2-57, and
160 ALL2-6, respectively. Chips from these experiments were embedded in epoxy bullets and sectioned by
161 with a diamond knife (in a microtome) to obtain a flat surface. Our goal with these measurements was
162 to confirm the accuracy of the calibration using orthogonal approaches of EELS and ESR, and to relate
163 the $Ti^{4+}/\Sigma Ti$ ratio to the fO_2 under which meteoritic hibonite formed or last equilibrated.

164 To test the efficacy of our calibration and apply it to meteoritic hibonite, we examined a CAI within
165 the CR2 chondrite NWA 5028 (thin section from the Center for Meteorite Studies, Arizona State
166 University collection #1845-5). The CAI was identified as a compact type-A (CTA) (Ramprasad et al.
167 2018). The hibonite grain is attached to the rim of the CAI (see the RS2 area in Ramprasad et al. 2018)

This is the peer-reviewed, final accepted version for American Mineralogist, published by the Mineralogical Society of America.
The published version is subject to change. Cite as Authors (Year) Title. American Mineralogist, in press.
DOI: https://doi.org/10.2138/am-2022-8311. http://www.minsocam.org/

and identified and quantified using a Cameca SX-100 electron microprobe, located in the Kuiper Materials Imaging and Characterization Facility (KMICF) at the Lunar and Planetary Laboratory, University of Arizona. A 1-µm probe with an acceleration voltage of 15 kV and beam current of 20 nA was used for the analyses, with counting times of 8 to 20 s on the peaks and 4 to 10 s on the background for each element. Mg, Na, Si and Al intensities were acquired on a TAP crystal; Ca, Ti, K, Cr, P and Cl on a PET crystal; and Fe, Mn and V on an LIF crystal. Petrographic description of the CAI is reported in Ramprasad et al. (2018).

We prepared electron-transparent cross sections of the four hibonite samples (3 synthetic and 1 meteoritic hibonite) using the ThermoScientific (formerly FEI) Helios NanoLab 660 G^3 focused-ion-beam scanning-electron microscope (FIB-SEM) also located in KMICF. The general procedures of FIB sample preparation, e.g., coarse cutting, lift out, and in situ thinning were previously described (Zega et al., 2007; 2020) but we note some exceptions briefly here. Rather than attach the FIB sections to Cu support grids in flagpole-style geometry, we used the top of one of the posts that has an M-shape configuration (Fig. S1b) to aid in securing the section on both sides and minimize bending. We created electron-transparent windows of 6 µm x 8 µm. Other areas of the synthetic hibonite FIB sections were kept thick ~500 nm, i.e., electron opaque. This mounting approach provided additional stability to the FIB section that was necessary in order to obtain very thin (<40 nm) samples for atomic-resolution analyses. All samples were ion polished down to 8 keV acceleration voltage to remove the amorphous damage layer on each surface created by higher-voltage milling (Schaffer et al. 2012).

STEM

The Ti standards and the natural and synthetic hibonites were measured using a 200 keV aberration-corrected Hitachi HF5000 scanning TEM (S/TEM). The HF5000 is equipped with a cold field-emission gun, a third-order spherical-aberration corrector for STEM mode, bright-field (BF), and

This is the peer-reviewed, final accepted version for American Mineralogist, published by the Mineralogical Society of America.
The published version is subject to change. Cite as Authors (Year) Title. American Mineralogist, in press.
DOI: https://doi.org/10.2138/am-2022-8311. http://www.minsocam.org/

192 annular dark field (ADF) STEM detectors, an Oxford Instruments X-Max N 100 TLE EDS system with
193 dual 100 mm^2 windowless silicon-drift detectors with solid angle (Ω) of 2.0 sr, and a Gatan Quantum
194 ER (model 965) electron energy-loss spectrometer (EELS). The Quantum ER is a Gatan Imaging Filter
195 (GIF) equipped with a 2048 × 2048 CCD detector and dual EELS capabilities for simultaneous
196 acquisition of low- and core-loss spectra. STEM-HAADF images were acquired using a 200 keV
197 acceleration voltage, a 10 μA emission current, and 3.45 eV extraction voltage, a STEM condenser
198 aperture of 25 μm, and a 2 μs dwell time.

199 Three types of EELS spectrum-imaging experiments were performed. These experiments include:
200 (1) large (30 × 30 nm up to 150 × 150 nm) field-of-view measurements to compare the Ti-oxide
201 standards and the hibonite samples (both natural and synthetic) under the same electron-optical
202 conditions; (2) large field-of-view (135 x 135 nm) measurements using a higher probe current and a
203 larger collection angle than in (1); and (3) atomic-resolution maps (field of view: 6.2 nm x 2.5 nm) of
204 the natural hibonite. Each experiment was performed in STEM mode using a similar condition as for
205 the HAADF images. All EELS spectra were corrected for channel-to-channel gain variation and dark
206 current. Each standard and synthetic sample was analyzed two times to verify the reproducibility of
207 results. For the standards, the two measurements represent different grains with different
208 orientations located in different areas on the lacey film of the TEM grid. For the synthetic hibonites,
209 spectra were acquired from different locations in the FIB section.

210 The experimental conditions for the EELS spectrum imaging are as follows. (1) For large field-of-
211 view analysis, the microscope was operated using a 100 pm probe, a STEM condenser aperture of 25
212 μm, a 105 pA probe current, and convergence angle (α) of 28 mrad. Spectra were acquired using an
213 EELS entrance aperture of 2.5 mm and a collection angle (β) of 24 mrad. The energy dispersion was set
214 to 0.025 eV/ch and a drift tube offset of 440 eV, enabling acquisition of the Ti $L_{2,3}$ edge with an energy
215 range of ~ 50 eV and analysis of its ELNES. At this scale, samples are not beam sensitive and the drift is

negligible. Therefore, maps were acquired with a single frame but a large pixel time of 2 s for core loss and 0.01 s for the low loss. Quantitative analysis was performed on summed spectra to enhance the signal-to-noise (S/N) ratio. (2) For EELS large field-of-view analysis, we used a different set of conditions because we wanted a quantifiable spectrum at each pixel. We used a condenser aperture size of 35 µm and a probe current of 330 pA. We increased β to 63 mrad by using high-angle EELS mode, which provides a shorter camera length than standard EELS mode. We also used a 5 mm EELS entrance aperture and a dispersion of 0.25 eV/channel to increase the EELS S/N ratio. Spectral images were acquired by averaging multiple passes (5 frames). A pixel time of 0.2 s for the core loss was used and 0.001 s for the low loss. (3) Atomic-resolution EELS requires lower probe current and shorter acquisition time to minimize the beam damage and the carbon deposition, respectively. Thus, we used a condenser aperture of 30 µm and reduced the probe current to 150 pA. Further, we used the liquid nitrogen cold trap on the HF5000 to limit the carbon deposition during beam rastering and to decrease the sample drift. We used a large EELS spectrometer aperture (5.0 mm), the high-angle EELS mode (β = 63 mrad), and a 0.5 eV/channel dispersion to ensure a high S/N ratio and short acquisition time. To obtain EELS spectra from individual atomic columns on the hibonite grain from the NWA 5028 meteorite, we oriented it along $[11\bar{2}0]$, with a goniometer tilt of α = 16.4° and β = -2.0°, enabling analysis of the stacking along [0001]. The drift tube offset was set at 400 eV, and EELS maps were acquired with a single frame, a pixel dwell time of 0.2 s for the core loss and 0.001 s for the low loss. These atomic-resolution experiments limited our acquisition time and probe current, and so EDS spectra could not be obtained at this scale of measurement.

Data Processing

Spectra were processed using personal Python scripts (available at: https://github.com/ZanettaPM/Ti-Oxidation-EELS-data-processing) constructed using Hyperspy (de la

Peña et al. 2021). The energy position of the low-loss and high-loss spectra from different pixels were calibrated via zero-loss peak (ZLP) centering. The average energy resolution calculated from the full-width-half-maximum intensity of the ZLP over all standard spectra (experimental condition 1) is approximately 0.26 eV. The π* peak of the C K-edge at 285 eV acquired with the same energy dispersion served as a calibration point. A shift of 1.7 eV is commonly observed at the π* peak energy (after ZLP centering) which corresponds to a ~2.5 eV shift at the Ti $L_{2,3}$ edge energy. An inverse power law (AE^{-r}) model, where E is the energy loss and A and r are constants, was used to subtract the background (random plural and single-scattering contributions). An energy window measuring 20 eV, placed between 430 eV and 450 eV (for a 0.025 eV/channel dispersion), was used to fit the background function. This range is located after potential ghost peak channels (due to the previous ZLP calibration) and at lower energy than possible Ti $L_{2,3}$ pre-edge peaks. The plural scattering contributions due to sample thickness were removed by Fourier-ratio deconvolution. We also removed the continuum beneath the white lines to isolate their intensities. There are varied methods for such removal, including a linear fit between edge onset and offset (Garvie and Buseck 1998; Zega et al. 2003), but for the purposes of reproducibility and consistency with previous work (Stoyanov et al. 2007) we applied a double-step function. The onset and the offset refer to the position at which the energy rapidly decreases to a ground-state intensity before the first peak and after the last peak in the Ti $L_{2,3}$ edge respectively. The double-step function was initially implemented by Van Aken and Liebscher (2002) for the Fe $L_{2,3}$ edge and later modified by Stoyanov et al. (2007) for Ti in the form of:

$$f(\mathrm{E})=h*\left(arctan\left(\left(\frac{\pi}{w}\right)*(\Delta E-E1)\right)+\frac{\pi}{2}\right)+h*\left(arctan\left(\left(\frac{\pi}{w}\right)*(\Delta E-E2)\right)+\frac{\pi}{2}\right) \quad (1)$$

where ΔE is the electron energy varying over a range of tens of eV; w represents the width of the functions fixed to 2 eV; E1 and E2 are the inflection points fixed at 457.5 and 463.0 eV, respectively;

and h is the height of the individual arctan functions. In this work, h is a free parameter fit to the spectrum after the L_2 edge between 473 and 477 eV depending on the shape of the offset (Giannini 2014).

EDS data were also processed using Hyperspy. We fit the spectra, i.e., background and peaks, using a linear combination of the different components and a least square minimization method. The model of the background and its implementation are described in Zanetta et al. (2019). Net peak counts are given by the Gaussian areas which allows us to obtain element maps. Quantification was achieved using the Cliff-Lorimer method (Cliff and Lorimer 1975) and an absorption-correction routine developed by Le Guillou et al. (2018) and based on Horita et al. (1987). We used theoretical k-factors provided by Oxford Instruments®. Hyperspectral maps, measuring about 0.4 µm² in area, with a pixel size of ~0.5 nm, were acquired with a dwell time of 30 µs during 1h. These maps were then binned to achieve a suitable S/N ratio, quantified, and recalculated as cation per formula unit (pfu). The first set of maps described below is 160 × 160 pixels and is used to display the elemental distributions of the cations. The second set of maps measures 10 × 10 pixels and is used to achieve a high number of counts and plot element variations. Major elements like Al reach 50,000 counts; Ca, Ti and Mg reach around 8,000 counts while minor elements like Fe and Si reach 1000 counts per pixel, per integrated peak. The high number of counts, the accurate fitting of the spectrum, and the absorption-correction procedure, which is particularly important to account for the thickness variation and the effect of heavy elements on lighter elements, allow us to give confident errors on the quantified results (less than 3% on major elements including Mg and Ti).

Experimental HAADF images were compared to simulated images computed using the QSTEM software, a multislice image-simulation code (Koch 2002). Two cases were investigated. We initially simulated a nominal hibonite ($CaAl_{12}O_{19}$). Then, using the Supercell software (Okhotnikov et al. 2016), we generated a hibonite solid solution of $CaAl_{10}Ti_1Mg_1O_{19}$ with Ti and Mg substituting on M4 sites and

This is the peer-reviewed, final accepted version for American Mineralogist, published by the Mineralogical Society of America.
The published version is subject to change. Cite as Authors (Year) Title. American Mineralogist, in press.
DOI: https://doi.org/10.2138/am-2022-8311. http://www.minsocam.org/

M3 sites, respectively with an occupancy of 0.5. We also investigated $CaAl_{10}Ti_1Mg_1O_{19}$ with Ti substituting between M2 and M4 sites. However, replicating the low concentration of Ti on the M2 site (<1 atom/unit cell for the M2 site, i.e., an occupancy of 0.5) is complex and requires a large supercell. So, for simplicity, we assumed in our QSTEM simulation that the M2 site contains only Al, and as discussed later, this assumption is valid (see Fig. 4b). From this hibonite structure, we simulated HAADF images to compare to our experimental HAADF images. We also added spherical aberration to our simulations of end-members: $CaAl_{12}O_{19}$ and $CaAl_{10}Ti_1Mg_1O_{19}$, accounting for the A1, B1, and C3 components of the aberration function, e.g., Urban et al. (1999) and Chang et al. (2006). The model consists of a 60×60×30 Å supercell. The scan window is 80×80 pixels with a resolution of 0.25 Å/pixel. We fixed the number of slices to 21 with a slice thickness of 1.43 Å.

Density Functional Theory

To understand the chemical shift and ELNES of our EELS spectra, we used density functional theory (DFT) to simulate spectra. We computed the electronic band structure of the Ti-oxides by means of the linearized augmented plane wave (LAPW) method, as implemented in the Wien2k package (Blaha et al. 2020). Electronic structure calculations of various Ti-bearing compounds were then conducted starting from experimentally reported crystal structures (Table 1). These structures are further relaxed by employing both local spin density approximation (LSDA) and the generalized gradient approach (GGA) (Perdew et al. 1996) exchange-correlation functionals. Both approaches are found to yield similar EELS spectra. Initialization parameters and self-consistent field (SCF) calculation convergence rules were set according to Hébert (2007). The energy to separate core and valence states were fixed at -6 Rydberg (Ry; 1 Ry ≈ 13.605 eV), except for $FeTiO_3$ and hibonite where values of -7 Ry and -8 Ry, respectively, were adopted because of their atomic configurations. After structural relaxation, we used an atomic sphere radius, i.e. muffin-tin radius (RMT), as large as possible but avoiding any

overlap. Within the RMT, the Wien2K code uses spherical harmonics, whereas in the interstitial region, plane waves are instead used. Final RMT values range from 1.63 to 1.99 atomic units (a.u.) for the Ti (Table 1). The matrix size RKmax ($R_{mt} * K_{max}$) was always fixed at 7.0, where K_{max} is the plane wave cutoff and R_{mt} is the smallest atomic sphere. Spin-polarized calculations were performed for Ti_2O_3, Ti_3O_5, and Ti_4O_7. Convergence criteria for the SCF cycle were fixed at 0.00001 Ry and 0.5 mRy/au for the energy and the force respectively. After optimization of the structure, we proceeded to the next iteration with higher k-mesh points (sampling points in the irreducible wedge of the first Brillouin zone of the material) until the theoretical electron energy-loss near-edge spectra (TELNES) between two iterations became nearly identical (peak positions and width differing by <0.1 eV). Final k-mesh sizes are presented in Table 1.

The TELNES3 program implemented in Wien2k was used to model EELS spectra (Jorissen 2007). Spectra were calculated using the same parameters as our experiments. We used a fixed splitting energy of 5.5 eV between the L_3 and L_2 transitions and a branching ratio (intensity ratio between the L_2 and L_3 lines) of 0.8 (Leapman et al. 1982; Stoyanov et al. 2007). We assumed no orientation dependence and so we averaged our calculations over all possible directions of the scattering vector with respect to the crystal. To improve the match between the model and the experimental results, we used 2×2×2 supercells. A full core-hole calculation for every species was achieved by removing one core electron that was later added to the valence electrons. The spectral broadening, which is mostly dependent on instrumental broadening, was always simulated with the same conditions, i.e., no linearly energy dependent valence broadening and spectrometer broadening set at 0.6 eV (experimentally determined). We kept the core-hole lifetime of the two edges as tabulated in the TELNES3 program.

We calculated EELS hibonite spectra for two Ti oxidation states. We investigated two cases with $Ti^{4+}/\Sigma Ti$ ratios of 1 and 0.5, respectively, and a composition of $CaAl_{10}Ti_1Mg_1O_{19}$, and $CaAl_9Ti_2Mg_1O_{19}$

This is the peer-reviewed, final accepted version for American Mineralogist, published by the Mineralogical Society of America.
The published version is subject to change. Cite as Authors (Year) Title. American Mineralogist, in press.
DOI: https://doi.org/10.2138/am-2022-8311. http://www.minsocam.org/

respectively. We produced the structures using the Supercell program (Okhotnikov et al. 2016). For the $Ti^{4+}/\Sigma Ti$ ratio of 1, we assumed that all the Ti occurs in the M4 site. For the ratio of 0.5, we randomly distributed the Ti between the M2 and M4 site with a 1:1 ratio. Mg is set to occupy the M3 site.

RESULTS

Chemical shift calibration and white-line ratio

We acquired EELS spectra at the Ti $L_{2,3}$ edge for standards to develop a calibration curve relating the white-line ratio to the $Ti^{4+}/\Sigma Ti$ ratio under the electron-optical conditions for our laboratory. Figure 1 shows the processed spectra normalized to the individual maxima acquired from Ti-bearing reference materials (the absolute intensity variations are normalized). The spectra show a chemical shift, marked by the edge onset, of 454.0 to 457.5 eV at the Ti $L_{2,3}$ edge that correlates with the valence state of the material. We observed doublets (labeled a, b and c, d) at the L_3 and L_2 edges similar to those reported by Stoyanov et al. (2007). The ELNES for these samples increases in complexity from reduced Ti^{2+} in TiO to oxidized Ti^{4+} in TiO_2. The spectrum of $CaTiO_3$, containing Ti^{4+}, shows four well-resolved broad peaks labeled a, b, c and d. In comparison, spectra from samples with mixed oxidation state display secondary peaks convoluted with the major ones. As the Ti-oxidation state decreases, peak intensity a and c decline in comparison to b and d peaks. The spectrum of TiO contains only two major peaks and low-intensity pre-peaks a and c (Table S1). The energy positions of the peaks (Table S2) are in agreement with previous measurements of Ti $L_{2,3}$ spectra of Ti-oxides (Leapman et al. 1982; Brydson et al. 1987, 1989; Henderson et al. 2002; Stoyanov et al. 2007).

Hibonite samples (synthetic and natural) that contain a high $Ti^{4+}/\Sigma Ti$ ratio (>0.8) also show four major peaks (a, b, c, and d) with secondary peaks on the b and the c peak. As shown in Fig. 2, the four spectra display ELNES features similar to the Ti-oxide standards. A shift in energy is visible from 458.05 to 458.4 eV at the a peak position (Table S3).

This is the peer-reviewed, final accepted version for American Mineralogist, published by the Mineralogical Society of America.
The published version is subject to change. Cite as Authors (Year) Title. American Mineralogist, in press.
DOI: https://doi.org/10.2138/am-2022-8311. http://www.minsocam.org/

Figure 3a shows the $I(L_2)/I(L_3)$ white-line intensity ratio as a function of Ti oxidation state for the standard reference materials and the synthetic hibonites after removal of background and continuum intensity and integration of 1 eV wide windows centered at energies of 455.8 and 465.25 eV (cf., Fig. 1 and 2). We obtained an exponential relationship between the $I(L_2)/I(L_3)$ and the $Ti^{4+}/\Sigma Ti$ ratios. Ti-oxide standards and synthetic hibonites with high $Ti^{4+}/\Sigma Ti$ values (>0.8) display strong (±50%) $I(L_2)/I(L_3)$ variation (Fig. 3a). To investigate the effect of the second window position on the IL_2/IL_3 ratio, we normalized all spectra to their individual maxima, and we plotted the value of the L_2 integration window as a function of the $Ti^{4+}/\Sigma Ti$ ratio (Fig. 3b). The data show significant scatter in the integrated intensity of the samples with a high $Ti^{4+}/\Sigma Ti$ ratio. We observe a general positive slope as a function of increasing Ti-oxidation state, but the large scatter in the data precludes a strong correlation between the white-line and $Ti^{4+}/\Sigma Ti$ ratios (Fig. 3a).

Comparison of experimental and simulated spectra

Given the complexities of the Ti $L_{2,3}$ ELNES, we performed first-principles calculations for the reference oxides and hibonites based on previous experimentally determined structures. The goal of these calculations is to verify the electronic-transition energies of the measured materials and to gain insight into the underlying physics. The input structure and parameters for the TELNES 3 calculations are presented in Table 1. To first order, the calculated spectra presented in Figure 4 match well to the experimental data. We observe the same peaks a through d in the simulated spectra (solid lines), giving reasonable 1:1 correspondence with experimental spectra (dashed lines). We observe that the chemical shift, peak position, and peak width are reproduced. What differs between experimental and simulated spectra is the peak heights. Even if the branching (L_3 to L_2) ratio of 0.8 is well reproduced (Leapman et al. 1982), the ratio of the doublets (i.e., a, b and c, d) are not consistent in certain spectra. In the experimental data, the peak a and c (corresponding to the $2t_{2g}$ level, see §4.1) are always less

intense than the peak b and d (3_{eg} level). In comparison, most of the calculated spectra (Ti_2O_3, Ti_4O_7, $FeTiO_3$, TiO_2 and $CaTiO_3$) exhibit the opposite trend. The most significant difference between the experimental and calculated spectra occurs for $CaTiO_3$. The calculated $CaTiO_3$ spectrum shows wider peaks and a significant peak-height variation compared to the experimental spectrum.

The hibonite model spectra shows similar results to the standard calculated spectra. The chemical shift is clearly visible in the calculated spectra for the two selected cases where $Ti^{4+}/\Sigma Ti=0.5$ and $Ti^{4+}/\Sigma Ti=1$ (Fig. 4b, red and purple curves, respectively). Compared to these calculated spectra, the experimental spectra with $Ti^{4+}/\Sigma Ti\sim0.9$ (ALL 2-6, ALL 2-57 and ALL 2-55 samples) display an edge onset energy located between these two endmembers (456.5 – 457.8 eV). Similar to the oxide standards, we find that the experimental ratios between the peaks a and b, and c and d are not reproduced by the calculation (cf., solid and dashed curves in Fig. 4). If calculated and experimental spectra are compared in more detail, the ELNES of the $Ti^{4+}/\Sigma Ti=1$ case where Ti is only located on the M4 site (purple curve) shows a close match to the experimental spectra. In comparison, the model in which $Ti^{4+}/\Sigma Ti=0.5$ and Ti is equally distributed between Al2 and Al4 sites (red curve) shows the presence of b" and d" peaks that are not observed in the experimental spectra.

Regardless of the specific site occupancies and those effects on the ELNES, our TELNES calculations show that the onset position of the Ti $L_{2,3}$ is predominantly dependent on the oxidation state. However, the position of the offset appears to depend on both the chemical shift and other crystal-field effects with peak position varying for similar $Ti^{4+}/\Sigma Ti$ values (e.g, peak d in $FeTiO_3$ vs TiO_2), which is corroborated in the experimental data (cf., Figs. 3a,b). These observations required us to develop a modified approach to quantify the $Ti^{4+}/\Sigma Ti$ ratio.

Edge onset correlation and coupled EELS/EDS NWA 5028 hibonite analysis

This is the peer-reviewed, final accepted version for American Mineralogist, published by the Mineralogical Society of America.
The published version is subject to change. Cite as Authors (Year) Title. American Mineralogist, in press.
DOI: https://doi.org/10.2138/am-2022-8311. http://www.minsocam.org/

As the onset position is only dependent on oxidation state for the Ti-bearing materials investigated in this study, we decided to explore its possible use for quantifying the $Ti^{4+}/\Sigma Ti$ ratio. Thus, we quantified the onset intensity (all spectra are normalized to their individual maxima) of the L_3 edge using a window of 2 eV ranging from 455 to 457 eV (Fig. 1 and 2. single window highlighted in blue) for the Ti-oxides. The window size and width were selected to give the best calibration (Fig. S3). We find that the L_3 integrated intensity decreases as a function of increasing oxidation state (Fig. 5). We fit the data to a polynomial function, which yields a 0.99 correlation coefficient (Fig 5). The obtained calibration was compared to the quantified $Ti^{4+}/\Sigma Ti$ ratios of previously synthesized hibonites (ALL series) and this led to a close match (Fig.5). Based on scattering of the data points from the oxide standards around the fitted curve, we estimate an absolute error of ~ 1% for the determination of the $Ti^{4+}/\Sigma Ti$ ratios (dashed black curves, Fig. 5).

A view of the complete CTA CAI and the local area from which the section of NWA 5028 was extracted is shown in Figure 6. We extracted a hibonite grain that occurs at the edge of the inner part of the rim layer (towards the core side of the CAI) with spinel and perovskite and is surrounded by a mixture of melilite and diopside. The hibonite grain contains up to 2 at% of Ti (8.3 wt% TiO_2) and Mg (2.4 wt% MgO), and low V 0.16 at % (0.56 wt% V_2O_3) (Table 2) and appears homogeneous in BSE contrast. Inclusions of spinel and perovskite are also observed in the grain. A large field-of-view STEM-HAADF image of the FIB section shows the hibonite grain and surrounding context (Fig. 7a). The absolute thickness of the lower-contrast zone is estimated to be <30 nm according to the method in Lakoubovskii et al. (2008). We oriented the Hib. 1 grain in Fig. 7a along $[11\bar{2}0]$, enabling imaging along [0001] (Fig. 7b). Analysis of an SAED pattern shows the 2.2 nm spacing along the [0001] direction (Fig. 7c), which appears in the lattice-fringe contrast of the HRTEM image (Fig. 7b). The SAED pattern reveals sharp and discrete reflections indicating local long-range order, free of stacking defects. However, stacking disorder (not shown) was observed in other locations. We focused our study on the

Hib. 1 hibonite grain in Fig. 7a, but measurements were also acquired from the Hib. 2 hibonite grain for comparison. We applied the new calibration curve to the Hib. 1 grain (Fig. 5). We obtained a mean $Ti^{4+}/\Sigma Ti$ value of 0.86±0.01 using the same acquisition procedure we applied to the standard oxides and synthetic hibonites. This value is in the same range as the orange hibonite from inclusion CG-11 of Allende or hibonite in the Blue Angel inclusion from Murchison (Beckett et al. 1988). This $Ti^{4+}/\Sigma Ti$ value is also comparable to those determined by Simon et al. (2009), Zega et al. (2012), Giannini (2014), and Han et al. (2021) even though their measurements were not based on a standard calibration.

In order to evaluate the homogeneity of the composition of the hibonite grain extracted from the CTA CAI of the NWA 5028 CR2 carbonaceous chondrite, we acquired simultaneous EDS and EELS spectra from the same area. We quantified each spectrum contained in every pixel of the EDS maps (Fig. 7a, white-dashed box, labeled Map. Fig. 8). Figure 8 shows the elemental distribution per formula unit (pfu) extracted from the X-ray lines present in the spectra of the map. The Ca map shows some spatial variations, likely due to the thickness of the sample, but the magnitude of variation is low and within error. In contrast, Ti and Mg exhibit significant spatial variations (0.65±0.03 to 0.8±0.04 cation pfu) and show inverse spatial correlations with Al. We note that Ti is quantified based on the Kα line which is not convoluted with any other line.

To further assess the mechanism at the origin of the Ti incorporation and gain insight into cation substitutions, we plotted four pertinent chemical fields based on quantified maps with the highest number of counts (10x10 pixels and thousand counts per peak; Fig. 9). Previous studies indicated that Ti can be incorporated into the structure either by direct substitution of Ti^{3+} for Al^{3+} or Ti^{4+} coupled substitution with Mg^{2+} for two Al^{3+}, and therefore we focused on these three elements (Allen et al. 1978; Beckett et al. 1988; Doyle et al. 2014; Berry et al. 2017). If cations are normalized to their sum, i.e. Al+Ca+Ti+Mg+V+Fe+Cr=13, we obtain values of Al=10.5±0.1, Ca=1±0.02 and O=19±0.5. Ti+Mg+V+Fe+Cr make up the 1.5 pfu difference. Si counts were near the detection limit (see Table 2;

Si=0.04 cation pfu and Fig. S4). Ca is homogeneous with a value close to 1 cation pfu, even as Al varies significantly. The Al concentration linearly decreases as Ti+Mg increases; a strong correlation with a slope ~-1.02 and R^2 = 0.9 is observed (Fig. 9a). The Ti and Mg concentrations spatially correlate (Fig. 8) but do not match perfectly (and anticorrelate with Al) with a range of 0.65 to 0.80 cations pfu (Fig. 9c). The concentration of Mg is approximately equivalent to Ti on average, but a significant dispersion around an ideal 1:1 correlation between Ti and Mg is observed (Fig. 9c). The Ca site shows a variation of ±0.02. In comparison, Ti and Mg (or Ti+Si and Mg+Fe) show a variation of ±0.15 cation pfu. Fe, Si, Cr and V are usually associated with the same substitution sites and can modify the relationship between Al and the other cations. Since Cr and V are negligible (Fig. S4) we plotted the effect of Fe and Si on the correlation (Fig. 9 d). Their low concentrations did not significantly affect the relationship (M2/M4 sites vs M3 site). We note that on average the concentration of Ti is approximately equivalent to Mg and the Ti+Si concentration is approximately equivalent to Fe+Mg as shown by the microprobe bulk measurement (Table 2). However, we emphasize that the nanoscale measurements reveal a significant heterogeneity that is not evidenced by the lower scale microprobe measurements.

EELS spectral images were acquired with EDS maps, and so we evaluated the Ti $L_{2,3}$ edge acquired over the same field of view. We quantified the chemical shift to obtain a $Ti^{4+}/\Sigma Ti$ ratio (Fig. 10) using our onset calibration (Fig. 5). The ratio varies from 0.78±0.04 to 0.93±0.04; note that the errors on these values are large due to the use of a smaller energy dispersion for this map (0.25 eV/channel vs 0.025 eV/channel). The map exhibits higher Ti^{3+} relative concentrations towards the grain boundary (cf., Fig. 7a). In comparison, the EELS spectrum image (not shown) of the hibonite grain in the top left corner of the FIB section (Fig. 7a) is homogeneous with a mean value of 0.95±0.04. We used the $Ti^{4+}/\Sigma Ti$ EELS ratio for assessing the electroneutrality of the sample. The ideal charge of 19 O pfu is subtracted from the charge of the cation sum, i.e., $Al^{3+}+Ti^{3+}+Ti^{4+}+Mg^{2+}+V^{3+}+Fe^{2+}+Cr^{3+}+Si^{4+}$. The observed distribution of Ti^{3+}, Ti^{4+} and Mg^{2+} and the low concentrations of other solutes (Fe, Cr, V, Si)

479 does not yield to electroneutrality, even if errors on quantification and possible variations in oxidation
480 states for the other solutes are considered (Fig. S7).

481 To evaluate the crystal chemistry and the atomic-scale variation of the $Ti^{4+}/\Sigma Ti$ ratio, we
482 performed aberration-corrected STEM-HAADF imaging. Such imaging reveals atomic columns
483 arranged in horizontal planes along the c-axis (Fig. 11). The planes are characterized by a high-contrast
484 central row of atomic columns juxtaposed by slightly less intense atomic columns above and below
485 (Fig. 11b,c). The atomic columns form an echelon-like motif that is repeated vertically along [0001]
486 (Fig. 11b,c).

487 Hibonite is a member of the magnetoplumbite group (Holtstam and Hålenius 2020). Its structure
488 can be described as a sequence of spinel blocks (or S-blocks) interspersed with conductor layers (or R-
489 blocks), which are visible in Fig. 11d (Nagashima et al. 2010). The Ca, O and Al sites (M1 to M5) are
490 represented with different colors (see the ball-and-stick model). The spinel block consists of the M1,
491 M3, and M5 sites (yellow, orange and green balls) giving a stoichiometry of Y_6O_8 where Y represents a
492 small cation like Al (see Doyle et al., 2014 for graphical representation). The R-Block contains large
493 cations such as Ca along with the M2 and M4 octahedral sites (red, light blue and dark blue), yielding
494 an overall composition of AY_6O_{11}, where A represents a large cation (Ca for instance). In hibonite, the
495 S- and R-blocks alternate, hence the final formula is $AY_{12}O_{19}$. In the model, the Ca atoms are shown in
496 red and match the central atom of the R-block in the HAADF image with the highest brightness (Fig.
497 11d). In this orientation (and in contrast to Han et al., 2021), Ca is adjacent to the M2 and M4 sites,
498 i.e., the light and dark blue spheres respectively in the model that complete the R-block (Fig. 11c, d, e,
499 f, g). The M1 and M3 sites occur in the darkest areas of the HAADF image, revealing clear separation of
500 each echelon-like motif (Fig. 11 f, g). Finally, the M5 columns (green spheres in the model) surround
501 the R-block and are visible as bright columns. In this orientation [11-20], every other M5 column is
502 brighter due to a higher atomic occupancy. The relatively darker M5 columns adjacent to the bright

M5 columns contain lower occupancy (50% lower in this direction). Light elements such as O are generally not detectable with HAADF imaging (see Carter and Williams, 2016) and are therefore not visible on the image simulation (Fig. 11d, f). The simulation accounting for the Ti and Mg substitutions and aberrations in Fig. 11g closely matches the experimental HAADF image (Fig.11c), in particular, reproducing the 'dumbbell' configuration where Ti atoms substitute onto the two adjacent M4 columns (white ellipses). The simulation of Mg substituting on the M3 site gives darker areas, reproducing the contrast observed in the HAADF image (Fig. 11c and 11g). The Ti concentration within the M2 site in this local area of the experimental image is below the detection limit.

We performed aberration-corrected STEM-EELS mapping of the local region of hibonite at its boundary with perovskite (Fig. 12) to determine its atomic-scale composition (cf., Fig. 7a). Our focus here is on Ti but because the Ca $L_{2,3}$ edge occurs at an energy close to that of Ti (346 eV and 456 eV, respectively), our energy dispersion allows the acquisition of both the Ca $L_{2,3}$ and Ti $L_{2,3}$ edges. We therefore mapped both cations. We note that the intensity of the Al L and K edges tend to be weak and located at lower and higher energy losses, (78 and 1560 eV, respectively) than Ca $L_{2,3}$ and Ti $L_{2,3}$ and are therefore not represented here. The O atoms, which are distributed throughout the structure are generally not detected with HAADF (although they can be observed using annular-bright-field STEM) and can be challenging to resolve by EELS, and so are also not represented here. The STEM-EELS mapping shows that the Ca columns are well defined (Fig.12b) and match well to the model with atoms in the center of the R-block (cf., Fig. 11c-g). All columns present relatively similar intensities suggesting that their occupancy is similar over the sampled area. The Ti $L_{2,3}$ map reveals that it occurs in the region of the M2 and the M4 sites adjacent to the Ca (Fig. 12c). The relative concentrations of Ti in M2 and M4 are difficult to determine by EELS, but the high-intensity pixels are distributed around the line defined by the Ca atoms, suggesting higher Ti concentration on the M4 site (Fig. 12c), as shown by the HAADF image simulation (Fig. 11g). We applied our edge onset calibration to the Ti $L_{2,3}$

edge to determine the $Ti^{4+}/\Sigma Ti$ ratio of this local area (Fig. 12d). The data show that the $Ti^{4+}/\Sigma Ti$ ratio is heterogeneous at the atomic scale with potentially more hotspots of higher Ti^{4+} in the center of the R block even if Ti^{3+} hotspots are also observed in the center of R-block in the bottom part of the map. We observe pure Ti^{4+} atomic columns but no pure Ti^{3+} columns.

DISCUSSION

Validity of the single-window method

In EELS, edges result from the transition of core electrons to unoccupied states above the Fermi level. The observed peaks in the Ti-oxide standards can mostly be explained by four possible ionizations. The interaction between the Ti 3d, 4s, and 4p atomic orbitals and oxygen 2s and 2p atomic orbitals gives rise to the following molecular orbital levels: $1a_{1g}(\sigma)$, $1t_{1u}(\sigma)$, $1e_g(\sigma)$, $2a_{1g}(\sigma)$, $2t_{1u}(\sigma)$, $2e_g(\sigma)$, $1t_{2g}(\pi)$, $3t_{1u}(\pi)$, $t_{2u}(\pi^0)$, $t_{1g}(\pi^0)$, $2t_{2g}(\pi^*)$,$3e_g(\sigma^*)$, $3a_{1g}(\sigma^*)$, $4t_{1u}(\sigma,\pi^*)$ (Fischer 1970; Stoyanov et al. 2007). In all of the Ti-oxides measured here, the molecular orbitals are filled up to the $t_{1g}(\pi^0)$. The dipole selection rules exclude the $4t_{1u}(\sigma, \pi^*)$ as a possible final state, and the $3a_{1g}(\sigma^*)$ level, at higher energy, is a lower probability transition. However, evidence of secondary peaks at 472 and 477 eV was observed in the TiO_2 spectrum that could correspond to $2p_{1/2}$,$2p_{3/2} \rightarrow 3a_{1g}$ transitions. The number and intensity of the Ti $L_{2,3}$ ELNES peaks are, therefore, mostly controlled by the $2p_{1/2}$,$2p_{3/2} \rightarrow 2t_{2g}(\pi^*)$,$3e_g(\sigma^*)$ transitions and the degree of occupancy of the $2t_{2g}$ level (Fig.1 and Table S1; Stoyanov et al. 2007).

In contrast to the oxide standards measured here, where Ti is restricted to one or two crystallographically distinct octahedral sites, hibonite has three distinct octahedra, M1 (point symmetry D3d), M4 (C3v) and M5 (Cs), a M3 tetrahedron (C3v), and the unusual fivefold-coordinated trigonal bipyramid M2 (D3h). Previous work suggested that Ti mostly occupies the M4 site (Beckett et al. 1988; Doyle et al. 2014, 2016; Ardit et al. 2016; Berry et al. 2017). Ti is therefore located in a site

551 with an octahedral coordination (except for low Ti concentration e.g., Berry et al., 2017) similar to the
552 Ti-oxide standards (Table 1). This similar Ti environment explains why ELNES of the Ti standards with
553 $Ti^{4+}/\Sigma Ti$ ratio=1 (TiO_2, $CaTiO_3$, and $FeTiO_3$) and the hibonite spectra show similar peak doublets.

554 The quantized electronic transitions mainly control the observed peak positions, e.g., Fig. 4.
555 However, previous work showed that ELNES are also affected by other interactions. For instance,
556 distortion of the Ti polyhedra, depending on the material, can add complexity to the Ti $L_{2,3}$ ELNES
557 (Stoyanov et al. 2007). The peak width, which depends on the time it takes for the ionized electron to
558 decay to the ground state, can also vary according to the electronic environment (Egerton 1996).
559 Decoupling the portion of the chemical shift due to the oxidation state is therefore challenging. The
560 white-line approach has the advantage of tracking the shift in energy as a mean to quantifying
561 oxidation-state ratios rather than precise fitting of the ELNES which is particularly challenging for early
562 3d metals that contain complex crystal-field effects superimposed on a chemical shift (Fischer 1970;
563 Leapman et al. 1982; De Groot et al. 1990; Brydson et al. 1993; Garvie and Buseck 1998; Stoyanov et
564 al. 2007). The white-line approach has been applied to 3d metals such as Fe (Van Aken et al. 1998; Van
565 Aken and Liebscher 2002) and Ti (Stoyanov et al. 2007). In the latter work, Stoyanov et al. (2007)
566 showed a relationship between the white-line intensity ratio (L_2/L_3) and the oxidation state of Ti. Thus,
567 we attempted a similar approach to obtain a calibration of the shift of the Ti $L_{2,3}$ edge as a function of
568 Ti oxidation state under the electron-optical conditions in our laboratory (Figure 1, 2, 3a). However,
569 because the Ti-oxide standards and synthetic hibonites with high $Ti^{4+}/\Sigma Ti$ values (>0.8) display large
570 (±50%) IL_2/IL_3 variations (Fig. 3a), the fit that we obtained is markedly different from the one reported
571 by Stoyanov et al. (2007). We attribute this difference to the position of the edge offset window (IL_2:
572 465.25 to 466.25 eV; cf., Fig. 1 and Fig. 3b). For standards with similar $Ti^{4+}/\Sigma Ti$ values (>0.8), we note
573 that the L_2 integration window (465.25 to 466.25 eV) can occur on the left side of the d peak, as can be
574 seen for $FeTiO_3$ and TiO_2 standards or directly on the crest as in $CaTiO_3$ (Fig.1). Thus, this difference in

position will significantly impact the final L_2 intensities and hence the IL_2/IL_3 white-line ratio. Moreover, our experimental results and DOS calculations demonstrate that the dependency of the edge-offset position on other effects, e.g., electronic structure, does not relate to our experimental microscope conditions (Fig. 4). These observations suggest that dependency of the white-line ratio on both oxidation and crystal-field effects complicates the development of a universal curve for Ti.

Difficulty in reproducing the white-line ratio method for Ti was also noted by Giannini (2014). As an alternative method, Giannini (2014) proposed using relative heights of the four peaks that occur in hibonite spectra as a possible proxy for the oxidation state. To tackle the crystal-field dependency, we first tried various methods that could relate the features present in the spectra to the oxidation state. Spectral parameters that are related to $Ti^{4+}/\Sigma Ti$, but not to the site occupancy, distortion, or Ti content would be ideal for a Ti-valence calibration curve. We therefore tested a variety of potential tracers for the valence state including: the position of the d peak (Fig. 2), the doublet dissociation in energy, the edge center energy (defined by the difference between the onset and the offset), the edge variance, and the relative heights (as proposed by Giannini (2014). We concluded however, that all of these parameters depend on effects other than just the chemical shift. The only alternative method leading to a satisfactory calibration curve was obtained when taking the ratio of the peak d energy range (464.5 to 468.5 eV) divided by the L_2 energy range (462.5 to 468.5) (Le Guillou et al. 2015). This method leads to a larger dispersion around the calibration curve but might be considered as an alternative if the S/N ratio of the acquisition is low (since it integrates energy ranges with higher intensities than the single window approach). The IL_3 onset window (455.8 to 456.8 eV) shows a more accurate correlation with the Ti oxidation state. We therefore used the IL_3 onset window for our $Ti^{4+}/\Sigma Ti$ calibration. However, the use of a wider window (455 to 457 eV) increases the final R^2 (Fig. 5) and reduces artifacts that are background related (Fig. S3). We note that the almost linear relationship between the IL_3 intensity and the $Ti^{4+}/\Sigma Ti$ ratio is linked to the evolution of the width of the band gap

for the various oxidation states. For TiO, which shows metallic conductivity, the conduction and the valence bands overlap, but for an insulator such as TiO_2 (or hibonite), the band gap becomes larger and the electronic screening poorer, leading to a shift to higher energy relative to metallic Ti.

As a test of the efficacy of the alternative method developed here, we find that the $Ti^{4+}/\Sigma Ti$ ratios of the ALL sample series quantified with our approach (Fig. 5) are ALL2-6=0.91±0.01, ALL2-57=0.88±0.01, and ALL2-55=0.84±0.01. These values compare favorably with the corresponding ratios of 0.95±0.01, 0.91±0.01, and 0.85±0.01, measured by Beckett et al. (1988) using electron spin resonance (ESR) spectroscopy. The agreement between the data sets from these orthogonal approaches and the lower data dispersion around the fitted curve in comparison to the previously discussed white-line ratio method suggests that the alternative method provides a higher accuracy under our optical conditions.

Error estimation on the bulk $Ti^{4+}/\Sigma Ti$ ratio determination and mapping limitations

The single-window method described above based on the edge-onset position requires that each spectrum must first be normalized to its own maximum to remove the intensity variations due to the sample thickness or Ti concentration. This normalization is possible because the d peak always corresponds to the maximum value of the spectra in the studied materials. The use of only one window in front of the edge potentially makes this method sensitive to the background noise especially for samples with high $Ti^{4+}/\Sigma Ti$ ratio (>0.8). Such noise sensitivity does not apply in the two-window method (e.g. Stoyanov et al., 2007) because at least one window is placed at energies where the signal/background (S/B) ratio is high (S/B>10). In comparison, the edge-onset method described here requires 1) a high S/B ratio (S/B>5) to avoid any noisy spike that would impact the integrated value and 2) correct removal of the background. The background should ideally fall to zero intensity

622 before the edge. To increase the reproducibility of $Ti^{4+}/\Sigma Ti$ quantification, we fixed the energy window
623 used for the background removal to a constant energy range and position (see the methods section).

624 For either the two-window method or our approach here, the calibration of the position of the
625 edge is essential. In our case, we fixed the π* peak of the C, K edge at 285 eV for the standard
626 calibration. Keeping the same dispersion and acquiring the C edge of amorphous carbon immediately
627 after the Ti edge maps provided reproducible measurements of the Ti edge with shift variations <0.04
628 eV between all the standard carbon π* peak positions. This protocol resulted in a small shift of about 2
629 eV of the Ti edge to lower energy among all the standards (Table S2). In comparison, Stoyanov et al.
630 (2007) used a dispersion of 0.3 eV/channel for the carbon calibration step and a dispersion of 0.05
631 eV/channel for the Ti edge acquisition. This difference in choice of dispersion is partly responsible for
632 why we obtain a different exponential calibration curve shown in Fig. 3a in comparison to Stoyanov et
633 al. (2007). The data show that standards define an error of ± 1.1 % around the calibration curve for a
634 dispersion of 0.025 eV/channel (Fig. 5). The $Ti^{4+}/\Sigma Ti$ ratio is therefore well constrained for bulk
635 measurements. This error is approximately similar to the 10% error on the Ti^{3+} wt% value determined
636 by Beckett et al. (1988) for values contained between 0.8 to 1 $Ti^{4+}/\Sigma Ti$. For lower $Ti^{4+}/\Sigma Ti$ values, our
637 approach presents a higher accuracy than ESR measurements (if the Ti^{3+} wt% increases relatively to
638 Ti^{4+}).

639 We find that errors on the $Ti^{4+}/\Sigma Ti$ ratio are larger for nanoscale mapping than for the bulk values
640 (experimental condition 1 in §2.2), which is mostly related to the larger energy dispersion. The higher
641 probe current and collection angle increase the S/N ratio and enable correct removal of the
642 background intensity, which are, as we note above, the main sources of uncertainties in this method.
643 The lower dispersion (0.25 ev/ch), however, gives lower spectral resolution and generates, therefore,
644 an inherently less accurate integration of the onset-position intensity. To determine the accuracy of
645 the $Ti^{4+}/\Sigma Ti$ ratio, we measured the Ti_3O_5 standard ($Ti^{4+}/\Sigma Ti$ ratio=0.5) with two different dispersions,

646 0.025 and 0.25 eV/channel (noted as experimental conditions 1 and 2 in §2.2). We estimate a
647 difference in the $Ti^{4+}/\Sigma Ti$ ratio between these two dispersions of ±0.04, which implies a relative error
648 of ±8% for the Ti_3O_5 standard and a ±5% relative error for $Ti^{4+}/\Sigma Ti$=0.86 in the NWA 5028 hibonite
649 grain.

650 Atomic-scale measurements are more complex than the nanoscale measurements described
651 above because the sample is beam-sensitive and carbon deposition can occur for exposure times
652 >0.2s. These experimental limitations force short acquisition times, which gives a lower S/N ratio than
653 in the nanoscale maps. The background is therefore noisier, leading to larger errors in the $Ti^{4+}/\Sigma Ti$ ratio
654 determination. This error is added to the error due to lower energy dispersion (0.5 eV/ch). Even
655 though the pre-edge background can be strongly affected by the noise, the S/N ratio of the Ti $L_{2,3}$ edge
656 is still above the detection limit and the shift is easily resolved (e.g., Fig. S5). The range of $Ti^{4+}/\Sigma Ti$
657 obtained at the atomic level is consistent with bulk values obtained on the same samples. Based on
658 the noise level, we estimate an absolute error in atomic scale maps of ±0.08 for the $Ti^{4+}/\Sigma Ti$
659 determination, which represents a relative error of ±12%. The bulk measurement allows an accurate
660 quantification of the mean $Ti^{4+}/\Sigma Ti$ value of the grain, whereas maps constrain variations in $Ti^{4+}/\Sigma Ti$
661 down to the atomic scale.

662

663 **Heterogeneities at the nanoscale**

664 The microprobe measurement (Table 2) of the hibonite that we extracted from the CAI in NWA
665 5028 gives a composition (Ca=1.0, Al=10.49 and Ti = 0.70 pfu and Mg ~ Ti) that is within the range of
666 previous measurements for meteoritic hibonites (e.g., Keil and Fuchs 1971; Allen et al. 1978;
667 Armstrong et al. 1982; MacPherson and Grossman 1984; Ihinger and Stolper 1986; Beckett et al. 1988;
668 Kööp et al. 2016), although it is Ti-rich (0.12 to 0.62 Ti pfu: Fig. S6 and Grossman 1975; Paque et al.
669 1987; Bischoff et al. 1993; Weber and Bischoff 1997; Srinivasan et al. 2000; Lin et al. 2003; Sapah

2015). Other solutes such as Fe, Si, Cr or V occur in relatively low concentration (<0.05 pfu), which simplifies the crystal chemistry of the hibonite in this CAI. However, hibonite grains in chondrites can exhibit heterogeneous compositions at the nanometer scale (Han et al. 2015, 2021; Doyle et al. 2016). Such variations reflect the spatial and temporal evolution of the thermodynamic conditions, i.e., chemical potential, temperature, and pressure of the system in which grains formed or last equilibrated. Our TEM data do show that the hibonite chemistry is heterogeneous at the nanoscale, which is particularly clear in the elemental maps for Ti, Mg and Al (Fig. 8 and 9). The plotted elemental compositions (Fig. 9) shows that Ca has negligible variation, whereas Al and Ti+Mg are anticorrelated, suggesting that Ti and Mg are only present on Al sites. We emphasize that the bulk sample exhibits approximately equal Mg and Ti concentrations (Table 2), but that compositional heterogeneities occur at the nanoscale for these two elements (Fig. 8 and 9c). The highlighting of such nanoscale heterogeneities could suggest that similar nanoscale variations occur in other hibonite grains.

Crystal chemistry and Ti substitution sites

The crystal chemistry of hibonite solid solutions, including description of the site occupancies, oxidation states of Mg, Ti, and other solutes is fundamental to the understanding of precise defect reactions that have occurred during the formation and equilibration of the phase. Recent studies showed that Ti mostly occupies the M4 site but that Ti^{4+} can also occupy the M2 site (Nagashima et al. 2010; Doyle et al. 2014; Berry et al. 2017; Asaduzzaman et al. 2021; Han et al. 2021). The Ti^{4+} distribution between the two sites is dependent on the Ti concentration (Berry et al. 2017).

In our hibonite DFT calculations, we set the Ti to the M4 site or homogeneously distribute it between the M2 site and the M4 site according to the literature (Doyle et al. 2014). Such relatively simple site distributions facilitate investigation of the effect of the Ti occupancy on the ELNES. In our calculations, the equal distribution of the Ti atoms on the M2 and M4 sites in hibonite gives a spectrum containing groups of peaks equal in intensity, e.g., b and b' (or d and d') and b'' (or d'', see

694 Fig. 4b, red spectrum). These ELNES features are not representative of the experimental spectra likely
695 because of the high concentration of Ti on the M2 site. Rather, a closest match between experimental
696 and simulated spectra, in terms of ELNES features, occurs where Ti occupies only the M4 site (%Ti^{4+}=1
697 case; Fig. 4b, purple spectrum). Therefore, the ELNES modelled by our DFT calculations confirm that Ti
698 mostly occupies the M4 site and that Ti is more concentrated on the M4 site rather than the M2 site,
699 consistent with previous observations and computational work (Doyle et al. 2014; Berry et al. 2017;
700 Asaduzzaman et al. 2021; Han et al. 2021).

701 In this study, the use of aberration corrected STEM coupled with image simulation and a
702 hyperspectral data-processing script developed in-house, allowed for the first time a direct
703 measurement of the Ti distribution between the M2 and M4 site in the hibonite structure (Fig. 11 and
704 12). STEM-HAADF images show brighter spots on the M4 site and the weaker intensity of the M3 sites.
705 The image simulations confirm that these features are due to the Ti and Mg substituting in M4 and M3
706 sites, respectively (Fig. 11). We did not observe strong contrast on the M2 position of the HAADF
707 image, suggesting this site contains a low concentration of Ti. Al and Ca sites exhibit homogeneous
708 intensities similar to the simulations (Fig 11 c). Vacancies may occur but are under the HAADF
709 simulation detection limit (2 to 3 at%).

710 EELS spectrum imaging of the Ca $L_{2,3}$ edge corroborates the STEM-HAADF data, i.e., homogeneous
711 intensity of the atomic columns, and suggests that there is no significant cation defect on the Ca site
712 (Fig 12 a, b). In comparison, the EELS spectrum image of the Ti $L_{2,3}$ edge shows high intensity pixels
713 that are dispersed around the Ca site. This dispersion around the Ca rows confirms the HAADF
714 measurements and indicates that Ti mostly occupies the two adjacent face-sharing octahedral M4
715 sites (which appear as dumbbells in projection). It was proposed that this configuration is energetically
716 favored due to stabilization of the Ti-Ti interaction (Doyle et al. 2014; Asaduzzaman et al. 2021). In
717 addition to the Ti substitution site determination, the data show that pure Ti^{4+} columns ($Ti^{4+}/\Sigma Ti$=1) are

This is the peer-reviewed, final accepted version for American Mineralogist, published by the Mineralogical Society of America.
The published version is subject to change. Cite as Authors (Year) Title. American Mineralogist, in press.
DOI: https://doi.org/10.2138/am-2022-8311. http://www.minsocam.org/

more abundant in the center of the row where the M2 sites are located (Fig. 12 d). Although the uncertainties on the $Ti^{4+}/\Sigma Ti$ ratio are larger at the atomic level than the nanoscale or bulk, the spatial distribution suggested by our STEM-EELS data indicate that if Ti^{4+} is distributed between the M2 and M4 sites, then Ti^{3+} mainly occupies the M4 site, which is consistent with previous work (Doyle et al. 2014). The observations made at the atomic scale allow us to discuss the mechanism of incorporation which we discuss below.

Mechanism of incorporation and Ti oxidation state

The observed crystal chemistry and the heterogeneities in conjunction with the knowledge of substitution mechanism(s) of solutes into the measured hibonites can shed light on the thermodynamic conditions that prevailed during condensation and subsequent alteration in the early solar nebula. Ti and Mg are the most concentrated solutes in chondritic hibonites (Brearley and Jones 1998), and the two key substitution reactions hypothesized for their incorporation are:

$$Ti(g) + Al_{Al}^{X} \rightleftharpoons Ti_{Al}^{X} + Al(g) \quad (2)$$

and

$$Ti(g) + Mg(g) + 2Al_{Al}^{X} \rightleftharpoons Ti_{Al}^{\cdot} + Mg_{Al}^{\prime} + 2Al(g) \quad (3)$$

Where Al_{Al}^{X} represents an aluminum ion sitting on an aluminum lattice site, with a Al^{3+} charge that define the reference state (Kröger and Vink 1956). $Ti_{Al}^{\cdot}$ is a titanium ion sitting on an aluminum lattice site, with a single positive charge (in comparison to the reference charge, i.e., 4+) and $Mg_{Al}^{\prime}$ a magnesium ion sitting on an aluminum lattice site, with a single negative charge (2+). In other words, in this equation (2), the cations are in the following valence state: Al^{3+}, Mg^{2+} and Ti^{4+}. Thus, coupling the analysis of the spatial distribution of Mg and Ti and its oxidation state is fundamental to testing the hypothesized substitution reactions in hibonite. Previous work showed that most meteoritic hibonite grains exhibit a nearly 1: 1 correlation of Mg:Ti (Allen et al. 1978; Armstrong et al. 1982;

This is the peer-reviewed, final accepted version for American Mineralogist, published by the Mineralogical Society of America.
The published version is subject to change. Cite as Authors (Year) Title. American Mineralogist, in press.
DOI: https://doi.org/10.2138/am-2022-8311. http://www.minsocam.org/

742 Doyle et al. 2014; Berry et al. 2017). This well-known 1:1 Mg:Ti correlation led previous workers to
743 conclude that reaction (3) was the main pathway for Ti (and Mg) incorporation (Allen et al. 1978;
744 Armstrong et al. 1982; Beckett et al. 1988; Han et al. 2021). The dispersion around the 1:1 line (Fig. 9c)
745 was also observed and attributed to a minor amount of Ti^{3+} being directly incorporated through
746 reaction (2) without Mg. Similarly, by plotting Si+Ti vs Fe+Mg, previous authors questioned the
747 incorporation mechanisms of Si and Fe (frequently present in the hibonite crystal chemistry) and their
748 impact on the 1:1 correlation (Simon et al. 2006, 2019; Han et al. 2015, 2021). Part of the dispersion
749 around the 1:1 curve (e.g., see Fig. 11b of Han et al. 2021), not explained by reaction (2) and (3), was
750 therefore interpreted as being due to secondary substitution of Fe^{2+} for Mg^{2+} and Si^{4+} for Ti^{4+} in parent
751 body settings.

752 In our study of this hibonite grain, several lines of evidence cannot be explained by a combination
753 of reactions (2) and (3), or by the incorporation of Fe and Si, and lead us to propose new mechanisms
754 of Ti and Mg incorporation into the hibonite structure. To be clear, we are not suggesting that
755 previously proposed mechanisms are not possible, but rather that they cannot explain the crystal
756 chemistry of the hibonite grain that we measure here. First, some points in Fig. 9c occur above the 1:1
757 correlation line and show that Mg is locally more concentrated than Ti which is unexpected if only
758 reaction (2) and (3) occur. Second, Fe and Si are in low concentrations, and so the magnitude of the
759 dispersion around the curve (Fig. 9d) cannot be explained by the substitution of these cations during a
760 secondary event as previously proposed Simon et al. (2006, 2019) and Han et al. (2015, 2021). Lastly,
761 the Ti oxidation state distribution of the NWA 5028 hibonite grain does not correlate with the Mg and
762 Ti distribution. If, as previously proposed in the literature, reaction (3) is predominant and the direct
763 substitution reaction (2) is responsible for the dispersion around the Ti:Mg 1:1 line, then the Ti
764 oxidation state should correlate with the Ti and Mg distribution. To highlight this discrepancy, we
765 calculated the excess of Mg (i.e., the ratio of Mg^{2+} relative to Ti^{4+} cations). Our data show that Mg is in

This is the peer-reviewed, final accepted version for American Mineralogist, published by the Mineralogical Society of America.
The published version is subject to change. Cite as Authors (Year) Title. American Mineralogist, in press.
DOI: https://doi.org/10.2138/am-2022-8311. http://www.minsocam.org/

766 excess in most of the pixels, and that a significant amount of Mg is therefore not associated with Ti^{4+}
767 (Fig. 13). These data indicate that part of Mg has been introduced independently from Ti into the
768 structure and that a portion of Ti^{4+} was reduced to Ti^{3+}.

769 Based on the EDS nanoscale quantification (Figs. 8 and 9) and the comparative EDS and EELS data
770 (Fig. 13), we infer that additional reactions must be considered to explain both the Mg concentration
771 and the Ti oxidation state distribution. If Mg substitutes independently in the structure, an oxygen
772 vacancy is locally formed to ensure local charge neutrality.

773 $$Mg(g) + Al_{Al}^{X} \rightleftharpoons Mg'_{Al} + v_o^{\cdot\cdot} + e' + Al(g) \quad (4)$$

774 $$O_o = v_o^{\cdot\cdot} + 2e' + {}^{1}/_{2}\ O_2 \quad (5)$$

775 (e.g, Kröger and Vink, 1956) where O_o represents an oxygen anion, $v_o^{\cdot\cdot}$ a doubly ionized oxygen
776 vacancy, and e' a free electron. If Mg substitutes near a Ti^{3+} already present in the structure, then the
777 Ti is oxidized to Ti^{4+}:

778 $$Mg(g) + Ti_{Al}^{X} + Al_{Al}^{X} \rightleftharpoons Mg'_{Al} + Ti_{Al}^{\cdot} + Al(g) \quad (6)$$

779 Lastly, we showed that Ti^{4+} could also be reduced to Ti^{3+} (Fig. 13) by trapping the free electrons
780 originating from the formation of oxygen vacancies (5), i.e.,

781 $$Ti_{Al}^{\cdot} + e' \rightleftharpoons Ti_{Al}^{X} \quad (7)$$

782 In order to test the hypothesis that oxygen vacancies could occur and play a key role in dictating
783 the concentration of Ti^{3+} (and the distribution of Ti and Mg) in the structure, similar to the mechanism
784 originally proposed by Beckett et al. (1988), we compared our Ti^{4+}/ΣTi maps to the total charge of the
785 cation sum subtracted by 19 O pfu (see §3.3). As noted, electroneutrality was not obtained, and we
786 find that the charge difference matches our Ti^{4+}/ΣTi maps (Fig. S7). Based on quantification of the
787 electroneutrality from our EDS and EELS data, we estimate that oxygen vacancies represent 0.25 to 0.5
788 pfu of the grain (Fig. S7). An oxygen vacancy of 0.5 pfu represents 1/12 of the atoms on the O4
789 Wyckoff site (which is the closest site to the M3 where Mg substitute) and 1 oxygen atom per unit cell

(which contains 38 oxygen atoms). Several additional pieces of evidence support that the charge difference is certainly due to O vacancies including: (1) neither Ca nor Al cation vacancies were observed in the experimental HAADF images, which was confirmed by comparison to the calculated images; (2) no abundant Ca vacancies were observed on the Ca $L_{2,3}$ EELS spectrum image; (3) other solutes (V, Cr, Fe) are in too low concentration to explain the charge difference; and (4) substitutions (2), (3), or (6) are unlikely to explain the $Ti^{4+}/\Sigma Ti$ distribution because the Mg/Ti and $Ti^{4+}/\Sigma Ti$ spatial distribution are not correlated (Fig. 8, 10 and 13).

We conclude that multiple reactions are needed to correctly describe the crystal chemistry of this specific hibonite grain including reactions producing oxygen vacancies. Therefore, the Ti oxidation state distribution in this grain is not only controlled by the Mg/Ti ratio, proposed previously for hibonite (Berry et al. 2017). As shown by reaction (6), the sequence of occurrence of these reactions is also important from the geological context and is discussed in detail in the next section. These multiple reactions preclude direct connection of $Ti^{4+}/\Sigma Ti$ to the fO_2 of the system. Instead, we suggest that the Ti (μ_{Ti}) and Mg chemical potential (μ_{Mg}) as well as the fO_2 of the gas play an important role in the final $Ti^{4+}/\Sigma Ti$ ratio recorded by the grain. Under reducing conditions, the fO_2 of the gas might prevail over the μ_{Mg}, whereas in oxidizing environment, the μ_{Mg} could prevail over the fO_2.

Cosmochemical Implications

NWA 5028 is a CR2 chondrite, and therefore, is not expected to have experienced high-temperature processing (thermal metamorphism with T> 400°C) on its parent body (Harju et al. 2014). In contrast, evidence for parent body aqueous alteration in the form of Fe-silicates within veins in spinel was observed in the chondrite (Ramprasad et al. 2018). However, we hypothesize that such low-temperature processes would not significantly modify the $Ti^{4+}/\Sigma Ti$ gradient or the total Ti/Mg ratio in hibonite over the timescales inferred for parent-body processing. We base this hypothesis on the

low diffusion rates of Ti and Mg in spinel (Brady and Cherniak 2010), which, as described in detail above, is a fundamental unit of the hibonite structure. Fe^{2+} could however exchange with Mg^{2+} and increase the diffusion rate of the two cations but the Fe concentration in this hibonite is low (<0.04 pfu) suggesting that Fe^{2+} did not replace a significant amount of Mg^{2+} (Simon et al. 2006, 2019). Thus, it is unlikely that parent-body processing impacted the parameters of interest in this study, and so we explore nebular processes below.

CAIs are classified into different types based on their mineralogy and morphology. Fluffy type-A (FTA) CAIs are melilite-rich objects that contain highly irregular and nodular structures and are believed to have been formed by gas-solid condensation in the early solar nebula. In comparison, CTAs exhibit more spheroidal shapes and are thought to have undergone partial to complete melting and recrystallization sometime after condensation but prior to incorporation into their parent bodies (MacPherson and Grossman 1984; Simon et al. 1999). The CAI selected here is typed as a CTA (Ramprasad et al. 2018). Therefore, at least two stages need to be considered as potential source of the heterogeneity in the grain (Fig. 9c and d). The grain could have incorporated homogeneous amounts of Ti and Mg that were later redistributed in the grain. Alternatively, the heterogeneity could have been directly inherited from the gas phase during initial condensation of the grain. Lastly, both scenarios could have occurred consecutively. We note that this hibonite grain is at the boundary of the Wark-Lovering (WL) rim (Fig. 6) and exhibits a low concentration of Si (Table 2), which suggests that this hibonite did not equilibrate with a silica-rich melt that might have formed from the secondary event that modified the morphology of the CTA. The heterogeneous Al, Ti, and Mg concentrations observed at the nanoscale (Fig. 8,9) as well as a $Ti^{4+}/\Sigma Ti$ gradient directed toward the grain boundary (away from the capping layer Fig. 7, 10) indicate that the thermal event that led to the chemical, structural, and morphological modification of the CAI was, locally, either too brief or at too low a temperature to fully re-equilibrate this hibonite grain with surrounding material.

838 The complex history recorded by this hibonite grain is shown schematically in Fig. 14. We consider
839 two scenarios. In scenario 1, the heterogeneity is inherited during nebular equilibration, i.e., before
840 the transient thermal event. 1.a) we hypothesize that the hibonite grain is formed through
841 backreaction with previously condensed material, in accordance with thermodynamic predictions,
842 producing a nominal $CaAl_{12}O_{19}$ composition; 1.b) Ti is incorporated at high temperature through a
843 direct substitution (reaction 2). 1.c) Mg solubility in hibonite increases as the temperature decreases
844 (e.g., Lodders, 2003) and is added through multiple reactions (4 and 6). Equilibrium between the grain
845 and the gas was not achieved and an elemental gradient was recorded, i.e., the grain became zoned in
846 Ti and Mg and $Ti^{4+}/\Sigma Ti$. 1.d) a transient thermal event occurred, presumably in the solar nebula but
847 prior to accretion of the CAI in its parent body. This secondary event may have remodified the Ti, Mg,
848 and $Ti^{4+}/\Sigma Ti$ distribution. For instance, if the fO_2 was sufficiently low during the thermal processing,
849 formation of new oxygen vacancies (reaction 5) could have led to the reduction of Ti^{4+} to Ti^{3+} via
850 reaction (7).

851 In the second scenario, both 2.a) solid-gas interaction or 2.b) a direct condensation of molecular
852 species to form the hibonite grain could have led to a homogeneous composition. Ti and Mg are
853 incorporated simultaneously through a coupled substitution (reaction 3 above) at high temperature
854 into the hibonite structure. Indeed, Doyle et al. (2014) showed that a local Mg^{2+} and Ti^{4+} association in
855 the structure (replacing two nearest Al^{3+}) are energetically favored in hibonite rather than the
856 formation of isolated defects (i.e., dissociated Ti and Mg atoms). If Ti facilitates the incorporation of
857 Mg at temperature higher than its normal condensation temperature (according to thermodynamic
858 predictions, e.g., Lodders, 2003), then it is likely that the Mg^{2+} and Ti^{4+} association (i.e., the coupled
859 substitution reaction 3) will dominate. A small amount of direct substitution reaction (2) could have
860 occurred. 2.c) At this stage, the Mg/Ti distribution matches the $Ti^{4+}/\Sigma Ti$ distribution and the 1:1
861 correlation still occurs in the grain. 2.d) The heterogeneity is inherited from the stage 2. The transient

thermal event impacting the CTA modifies the distribution of Ti and Mg and oxygen vacancies are formed. The $Ti^{4+}/\Sigma Ti$ is modified by reaction (7) reducing Ti^{4+} in the structure to Ti^{3+}. The 1:1 Mg:Ti correlation is lost and the Ti and Mg distributions do not match the $Ti^{4+}/\Sigma Ti$ distribution.

It is difficult to conclude whether scenario 1 or 2 is the correct interpretation for the history of this grain because thermodynamic models of Mg and Ti in hibonite are not available in the literature. Thermodynamic equilibrium calculations predict hibonite forms as a relatively pure Ca-Al-oxide. Therefore, measurement of hibonite grains extracted from FTA CAIs and the development of a more comprehensive thermodynamic model would be important steppingstones in understanding which scenario occurred for this grain and what such defects can tell us about the conditions in which hibonite formed or last equilibrated.

Hibonite as nebular oxygen barometer?

Hibonite is among the first several phases thermodynamically predicted to form in a gas of solar composition (Yoneda and Grossman 1995; Ebel and Grossman 2000; Lodders 2003). According to such models, corundum (Al_2O_3) which is calculated to condense first, can back react with Ca (as atomic Ca or molecular CaO) in the nebular gas to form hibonite. If the hibonite grain equilibrates with the gas, then the $Ti^{4+}/\Sigma Ti$ in hibonite should reflect the T, P, and fO_2 of the system. It was proposed that under sufficiently oxidizing conditions, the $Ti^{4+}/\Sigma Ti$ in hibonite is linearly correlated to the oxygen fugacity (fO_2) of the environment in which it formed (Beckett et al. 1988). This relationship was established assuming that: 1) most of the Ti in hibonite is Ti^{4+} and incorporated through the coupled substitution reaction (3) and 2) Ti^{4+} was reduced to Ti^{3+} by trapping free electrons originating from the formation of oxygen vacancies (reactions 5 and 7). In their study, Beckett et al., (1988) investigated this relationship for specific hibonite compositions, i.e., with homogeneous Mg concentrations and hence a fixed chemical Mg potential (μ_{Mg}). In comparison, Doyle et al. (2014) and Berry et al. (2017), argued that the

886 Ti^{3+} concentration in the hibonite structure is directly dependent on the Mg activity in the gas
887 (reaction 7) and that Ti^{4+}/ ΣTi might be independent of the fO_2. This scenario implies that in the
888 absence of Mg, all Ti in hibonite must be Ti^{3+}. We note that in their studies they investigated fO_2
889 conditions similar to those synthesized by Beckett et al. (1988) but on samples with different Mg
890 concentrations, i.e., variable μ_{Mg}. Thus, moving forward, we underline three uncertainties that must be
891 resolved for hibonite to be used as an oxybarometer.

892 First, the analysis of hibonite in the CTA from NWA 5028 reveals that Mg played a key role in the Ti
893 oxidation state recorded by the hibonite grain. The final Mg concentration must therefore be
894 considered because the relationship between Ti^{4+}/ΣTi and fO_2 will depend on the availability of Mg
895 according to reaction (4). The synthesis of hibonite matching the compositions of specific samples (BA
896 and ALL samples) allowed Beckett et al. (1988) to determine a relationship for a specific set of
897 conditions and a fixed Mg chemical potential. Thus, understanding the relationship of Ti^{4+}/ΣTi and fO_2
898 in other hibonite samples, with different compositions, requires knowledge of the μ_{Mg}.

899 Another complexity in relating Ti^{4+}/ΣTi and the fO_2 is that numerous 3d metals can substitute into
900 the hibonite crystal, i.e., Fe, Cr, V (Allen et al. 1978; Beckett et al. 1988; Bermanec et al. 1996;
901 Rakotondrazafy et al. 1996; Simon et al. 1997). Of these, V can occur in relatively high concentration in
902 certain types of CAIs, e.g., the blue angel inclusion from Murchison that contains up to 1.8 wt% V_2O_3
903 (Armstrong et al. 1982). If, e.g., V^{3+} or V^{4+} compete with Ti for similar Al sites, the measured Ti^{4+}/ΣTi
904 ratio alone will not be representative of the fO_2 of the material when it last equilibrated. Other
905 elements can also compete with Ti in meteoritic hibonites. Even if they occur in lower abundance than
906 V, the estimation of their concentration is also important to establishing the relationship between
907 Ti^{4+}/ΣTi and the fO_2.

908 In addition, the fO_2 variation as a function of temperature should be considered. For Ti^{4+}/ΣTi to be
909 useful in constraining redox conditions for natural hibonites, the temperature pathway experienced by

the grain would ideally be known. For example, the temperature of formation and hence fO_2 of a hibonite grain extracted from an FTA CAI preserving primary signatures of condensation could be estimated based on equilibrium thermodynamic predictions. However, the case of a CTA CAI, as measured here, is more complex. On the one hand, it is likely that kinetics played an important role on the recorded Ti-oxidation state during the brief and intense thermal processing that the CTA may have experienced, precluding correlation of the $Ti^{4+}/\Sigma Ti$ ratio to the fO_2 without an appropriate kinetic model. On the other hand, the elemental and the oxidation gradients could be used to determine the time–temperature path associated with the diffusion process from profile modeling (Cuvillier et al. 2015). However, the temperature and the duration of thermal processing of this CTA CAI was not estimated because it requires disentangling if the zonation was inherited from growth during condensation or because of diffusion in a subsequent event. Deciphering these signatures is beyond the scope of this paper.

Developing methods to quantify the nebular fugacity is challenging because the entire crystal chemistry, including all possible crystal defects, must be known. A complete model considering the parameters discussed above, e.g., μ_{Mg}, temperature history, the solutes competing with Ti, and the reaction paths for Ti incorporation would give a correct estimation of the fO_2 of the gas in which the grain formed or last equilibrated. Such a model will be the subject of a future paper.

CONCLUSIONS

We developed an EELS method to measure the $Ti^{4+}/\Sigma Ti$ ratio of oxide materials at various spatial scales. Experimental data, supported by first-principles DFT calculations, confirm that use of the EELS Ti $L_{2,3}$ edge onset is suitable to quantify Ti-oxidation states in heterogeneous materials. By coupling STEM-EDS and -EELS and applying them to measurement of a hibonite grain from a CTA CAI extracted from the NWA 5028 CR2 chondrite, we constrained the hibonite chemistry. The grain is zoned, with Al

and Ti anticorrelating, and Ti occurring as both Ti^{3+} and Ti^{4+}. Further, applying our developed quantitative EELS method at the atomic scale, we find that the Ti^{3+} mainly occupies the M4 site, Ti^{4+} is distributed between the M2 and M4 sites with a preference for M4, and Mg occupies M3. From the crystal chemistry, we infer that multiple reaction paths incorporated both Ti and Mg, and that coupled substitution is not the only reaction incorporating these cations into the hibonite structure. The formation of oxygen vacancies in a reducing nebular gas impacted the concentration of the reduced Ti. We conclude that the observed zoning testifies to a complex history in which hibonite may have been witness to large changes in nebular oxygen fugacity. However, the use of hibonite as an oxybarometer via measurement of its $Ti^{4+}/\Sigma Ti$ ratio alone is made complicated by its crystal chemistry, the solutes that can compete with Ti, and the varied reaction paths for Ti incorporation. We show that the μ_{Ti}, μ_{Mg}, and fO_2 of the system, play an important role in the final $Ti^{4+}/\Sigma Ti$ ratio recorded by the grain. Depending on the redox conditions of the system, the fO_2 or the μ_{Mg} could prevail. Thus, careful measurement of these variables and consideration of the reaction paths are essential. An approach combining measurements and modelling of the kind we report here could allow for more widespread use of hibonite (and other phases) as direct probes of the thermodynamic landscape of the early solar nebula.

ACKNOWLEDGEMENTS

Research supported by the NASA Emerging Worlds (80NSSC19K0509) and Laboratory Analysis of Returned Samples (80NSSC18K1475) Programs. We also thank Dr. Lindsay Keller for the Ti_4O_7 powder. The DFT results are based upon High Performance Computing (HPC) resources supported by the University of Arizona TRIF, UITS, and Research, Innovation, and Impact (RII) and maintained by the UArizona Research Technologies department. We gratefully acknowledge NASA (grants #NNX12AL47G and #NNX15AJ22G) and NSF (grant #1531243) for funding of the instrumentation in the Kuiper

958 Materials Imaging and Characterization Facility at the Lunar and Planetary Laboratory, University of
959 Arizona. We thank members of the Planetary Materials Research Group at LPL for helpful discussions.
960 P-M. Z. thanks Dr. Kenneth Domanik for his help with microprobe measurements.

961

962

963

964 # REFERENCES CITED

965 Afir, A., Achour, M., and Saoula, N. (1999) X-ray diffraction study of Ti-O-C system at high temperature
966 and in a continuous vacuum. Journal of Alloys and Compounds, 288, 124–140.
967 Allen, J.M., Grossman, L., Davis, A.M., and Hutcheon, I.D. (1978) Mineralogy, textures and mode of
968 formation of a hibonite-bearing Allende inclusion. Lunar and Planetary Science Conference
969 Proceedings, 9, 1209–1233.
970 Amelin, Y., Connelly, J., Zartman, R.E., Chen, J.H., Göpel, C., and Neymark, L.A. (2009) Modern U-Pb
971 chronometry of meteorites: Advancing to higher time resolution reveals new problems.
972 Geochimica et Cosmochimica Acta, 73, 5212–5223.
973 Ardit, M., Borcănescu, S., Cruciani, G., Dondi, M., Lazău, I., Păcurariu, C., and Zanelli, C. (2016) Ni-Ti
974 Codoped Hibonite Ceramic Pigments by Combustion Synthesis: Crystal Structure and Optical
975 Properties. Journal of the American Ceramic Society, 99, 1749–1760.
976 Armstrong, J.T., Meeker, G.P., Huneke, J.C., and Wasserburg, G.J. (1982) The Blue Angel: I. The
977 mineralogy and petrogenesis of a hibonite inclusion from the Murchison meteorite. Geochimica
978 et Cosmochimica Acta, 46, 575–595.
979 Asaduzzaman, A., Muralidharan, K., and Zega, T.J. (2021) Density Functional Theory Driven Analysis of
980 the Interplay among Structure, Composition, and Oxidation State of Titanium in Hibonite, Spinel,
981 and Perovskite. ACS Earth and Space Chemistry, acsearthspacechem.0c00309.
982 Azaroff, L. V., and Pease, D.M. (1974) X-ray absorption spectra. X-ray Spectroscopy.
983 Beckett, J.R., Live, D., Tsay, F.D., Grossman, L., and Stolper, E. (1988) Ti3+ in meteoritic and synthetic
984 hibonite. Geochimica et Cosmochimica Acta, 52, 1479–1495.
985 Bermanec, V., Holtstam, D., Sturman, D., Criddle, A.J., Back, M.E., and Šćavničar, S. (1996) Nežilovite, a
986 new member of the magnetoplumbite group, and the crystal chemistry of magnetoplumbite and
987 hibonite. Canadian Mineralogist, 34, 1287–1297.

988 Berry, A.J., Schofield, P.F., Kravtsova, A.N., Miller, L.A., Stephen, N.R., Walker, A.M., Soldatov, A. V.,
989 Ireland, T.R., Geraki, K., and Mosselmans, J.F.W. (2017) The limitations of hibonite as a single-
990 mineral oxybarometer for early solar system processes. Chemical Geology, 466, 32–40.
991 Bischoff, A., Palme, H., Ash, R.D., Clayton, R.N., Schultz, L., Herpers, U., Stöffler, D., Grady, M.M.,
992 Pillinger, C.T., Spettel, B., and others (1993) Paired Renazzo-type (CR) carbonaceous chondrites
993 from the Sahara. Geochimica et Cosmochimica Acta, 57, 1587–1603.
994 Blaha, P., Schwarz, K., Tran, F., Laskowski, R., Madsen, G.K.H., and Marks, L.D. (2020) WIEN2k: An
995 APW+lo program for calculating the properties of solids. Journal of Chemical Physics, 152,
996 074101.
997 Brady, J.B., and Cherniak, D.J. (2010) Diffusion in Minerals: An Overview of Published Experimental
998 Diffusion Data. Reviews in Mineralogy and Geochemistry, 72, 899–920.
999 Brearley, A.J., and Jones, R.H. (1998) Chondritic meteorites. Reviews in Mineralogy and Geochemistry,
1000 36, 3–398.
1001 Brydson, R., Williams, B.G., Engel, W., Sauer, H., Zeitler, E., and Thomas, J.M. (1987) Electron energy-
1002 loss spectroscopy (EELS) and the electronic structure of titanium dioxide. Solid State
1003 Communications, 64, 609–612.
1004 Brydson, R., Sauer, H., Engel, W., Thomass, J.M., Zeitler, E., Kosugi, N., and Kuroda, H. (1989) Electron
1005 energy loss and x-ray absorption spectroscopy of rutile and anatase: A test of structural
1006 sensitivity. Journal of Physics: Condensed Matter, 1, 797–812.
1007 Brydson, R., Garvie, L.A.J., Craven, A.J., Sauer, H., Hofer, F., and Cressey, G. (1993) L2,3 edges of
1008 tetrahedrally coordinated d0 transition-metal oxyanions XO4n-. Journal of Physics: Condensed
1009 Matter, 5, 9379–9392.
1010 Cameron, A.G.W. (1962) Formation of the solar nebula. Icarus, 1, 339–342.
1011 Carter, C.B., and Williams, D.B. (2016) Transmission Electron Microscopy: Diffraction, Imaging, and

1012 Spectrometry, 1–518 p. Springer.

1013 Chang, L.Y., Kirkland, A.I., and Titchmarsh, J.M. (2006) On the importance of fifth-order spherical
1014 aberration for a fully corrected electron microscope. Ultramicroscopy, 106, 301–306.

1015 Chi, M., Ishii, H.A., Simon, S.B., Bradley, J.P., Dai, Z., Joswiak, D., Browning, N.D., and Matrajt, G. (2009)
1016 The origin of refractory minerals in comet 81P/Wild 2. Geochimica et Cosmochimica Acta, 73,
1017 7150–7161.

1018 Cliff, G., and Lorimer, G.W. (1975) The quantitative analysis of thin specimens. Journal of Microscopy,
1019 103, 203–207.

1020 Connelly, J.N., Bizzarro, M., Krot, A.N., Nordlund, Å., Wielandt, D., and Ivanova, M.A. (2012) The
1021 Absolute Chronology and Thermal Processing of Solids in the Solar Protoplanetary Disk. Science,
1022 338, 651–655.

1023 Connolly, H.C., and Burnett, D.S. (2003) On type B CAI formation: Experimental constraints on fO2
1024 variations in spinel minor element partitioning and reequilibration effects. Geochimica et
1025 Cosmochimica Acta, 67, 4429–4434.

1026 Curien, H., Guillemin, C., Orcel, J.T., and Sternberg, M. (1956) La hibonite, nouvelle espèce minérale.
1027 Comptes Rendus Hebdomadaires des Seances de l'Academie des Sciences, 242, 2845–2847.

1028 Cuvillier, P., Leroux, H., Jacob, D., and Hirel, P. (2015) Fe-Mg interdiffusion profiles in rimmed forsterite
1029 grains in the Allende matrix: time--temperature constraints for the parent body metamorphism.
1030 Meteoritics & Planetary Science, 50, 1529–1545.

1031 De Groot, F.M.F., Fuggle, J.C., Thole, B.T., and Sawatzky, G.A. (1990) L q 3 x-ray-absorption edges of d
1032 compounds: K+, Ca2+, Sc'+, and Ti + in Oh (octahedral) symmetry, 15 p. PHYSICAL REVIEW Vol. 8.

1033 de la Peña, F., Prestat, E., Fauske, V.T., Burdet, P., Furnival, T., Jokubauskas, P., Nord, M., Ostasevicius,
1034 T., Lähnemann, J., MacArthur, K.E., and others (2021) hyperspy/hyperspy: Release v1.6.3.

1035 Doyle, P.M., Schofield, P.F., Berry, A.J., Walker, A.M., and Knight, K.S. (2014) Substitution of Ti3+ and

Ti4+ in hibonite (CaAl12O19). American Mineralogist, 99, 1369–1382.

Doyle, P.M., Berry, A.J., Schofield, P.F., and Mosselmans, J.F.W. (2016) The effect of site geometry, Ti content and Ti oxidation state on the Ti K-edge XANES spectrum of synthetic hibonite. Geochimica et Cosmochimica Acta, 187, 294–310.

Ebel, D.S. (2006) Condensation of Rocky Material in Astrophysical Environments IN: Meteorites and the Early Solar System (ed. D.S. Lauretta and H.Y. McSween). University of Arizona Press, 253–277.

Ebel, D.S., and Grossman, L. (2000) Condensation in dust-enriched systems. Geochimica et Cosmochimica Acta, 64, 339–366.

Egerton, R.F. (1996) Electron Energy-Loss Spectroscopy in the Electron Microscope, 3rd editio. (Springer, Ed.)Electron Energy-Loss Spectroscopy in the Electron Microscope.

Fischer, D.W. (1970) Molecular-Orbital Interpretation of the Soft X-Ray L II,III Emission and Absorption Spectra from Some Titanium and Vanadium Compounds Band Structure and the Titanium L II, III X-Ray Emission and Absorption Spectra from Pure. Journal of Applied Physics, 41, 3561.

Garvie, L.A.J., and Buseck, P.R. (1998) Ratios of ferrous to ferric iron from nanometre-sized areas in minerals. Nature, 396, 667–670.

Garvie, L.A.J., Craven, A.J., and Brydson, R. (1994) Use of electron-energy loss near-edge fine structure in the study of minerals. American Mineralogist, 79, 411–425.

Giannini, M. (2014) The crystal chemistry of hibonite: an indicator for oxygen fugacity during Solar nebula condensation? Thesis.

Grossman, L. (1972) Condensation in the primitive solar nebula. Geochimica et Cosmochimica Acta, 36, 597–619.

Grossman, L. (1975) Petrography and mineral chemistry of Ca-rich inclusions in the Allende meteorite. Geochimica et Cosmochimica Acta, 39, 433–454.

Grossman, L., Beckett, J.R., Fedkin, A. V., Simon, S.B., and Ciesla, F.J. (2008) Redox conditions in the solar nebula: Observational, experimental, and theoretical constraints. Reviews in Mineralogy and Geochemistry, 68, 93–140.

Han, J., Brearley, A.J., and Keller, L.P. (2015) Microstructural evidence for a disequilibrium condensation origin for hibonite-spinel inclusions in the ALHA77307 CO3.0 chondrite. Meteoritics & Planetary Science, 50, 2121–2136.

Han, J., Ohnishi, I., Yasuhara, A., and Keller, L.P. (2021) Atomic-scale structure and non-stoichiometry of meteoritic hibonite: a transmission electron microscope study. American Mineralogist.

Harju, E.R., Rubin, A.E., Ahn, I., Choi, B.-G.G., Ziegler, K., and Wasson, J.T. (2014) Progressive aqueous alteration of CR carbonaceous chondrites. Geochimica et Cosmochimica Acta, 139, 267–292.

Hébert, C. (2007, January 1) Practical aspects of running the WIEN2k code for electron spectroscopy. Micron. Elsevier Ltd.

Henderson, G.S., Liu, X., and Fleet, M.E. (2002) A Ti L-edge X-ray absorption study of Ti-silicate glasses. Physics and Chemistry of Minerals, 29, 32–42.

Holtstam, D., and Hålenius, U. (2020) Nomenclature of the magnetoplumbite group. Mineralogical Magazine, 84, 376–380.

Horita, Z., Sano, T., and Nemoto, M. (1987) Simplification of X-ray absorption correction in thin-sample quantitative microanalysis. Ultramicroscopy, 21, 271–276.

Iakoubovskii, K., Mitsuishi, K., Nakayama, Y., and Furuya, K. (2008) Thickness measurements with electron energy loss spectroscopy. Microscopy Research and Technique, 71, 626–631.

Ihinger, P.D., and Stolper, E. (1986) The color of meteoritic hibonite: an indicator of oxygen fugacity. Earth and Planetary Science Letters, 78, 67–79.

Jorissen, K. (2007) The ab initio calculation of relativistic electron energy loss spectra. Ph. D. thesis.

Keil, K., and Fuchs, L.H. (1971) Hibonite [Ca2(Al, Ti)24O38] from the Leoville and Allende chondritic

meteorites. Earth and Planetary Science Letters, 12, 184–190.

Keller, L.P. (1995) TRANSMISSION ELECTRON MICROSCOPE STUDIES OF EXTRATERRESTRIAL MATERIALS. Final Technical Report for NASA Contract:NAS 9-18992.

Keller, L.P., and Buseck, P.R. (1994) Twinning in meteoritic and synthetic perovskite. American Mineralogist, 79, 73–79.

Koch, C. (2002) DETERMINATION OF CORE STRUCTURE PERIODICITY AND POINT DEFECT DENSITY ALONG DISLOCATIONS. Dissertation.

Kööp, L., Nakashima, D., Heck, P.R., Kita, N.T., Tenner, T.J., Krot, A.N., Nagashima, K., Park, C., and Davis, A.M. (2016) New constraints on the relationship between 26Al and oxygen, calcium, and titanium isotopic variation in the early Solar System from a multielement isotopic study of spinel-hibonite inclusions. Geochimica et Cosmochimica Acta, 184, 151–172.

Kröger, F.A., and Vink, H.J. (1956) Relations between the Concentrations of Imperfections in Crystalline Solids. Solid State Physics - Advances in Research and Applications, 3, 307–435.

Larimer, J.W. (1967) Chemical fractionations in meteorites-I. Condensation of the elements. Geochimica et Cosmochimica Acta, 31, 1215–1238.

Le Guillou, C., Changela G., H., and Brearley, A.J. (2015) Widespread oxidized and hydrated amorphous silicates in CR chondrites matrices: Implications for alteration conditions and H2 degassing of asteroids. Earth and Planetary Science Letters, 420, 162–173.

Le Guillou, C., Leroux, H., Zanetta, P.M., Brearley, A.J., De La Pena, F., and Marinova, M. (2018) Water Content in Amorphous Silicates of Chondrite Matrices Determined by Advanced TEM Analysis---And Scanning Transmission X-Ray Microscopy. In Lunar and Planetary Science Conference Vol. 49.

Leapman, R.D., Grunes, L.A., and Fejes, P.L. (1982) Study of the L23 edges in the 3d transition metals and their oxides by electron-energy-loss spectroscopy with comparisons to theory. Physical

Review B, 26, 614–635.

Lewis, J.S. (1974) The temperature gradient in the solar nebula. Science, 186, 440–443.

Lin, Y., Kimura, M., and Wang, D. (2003) Fassaites in compact type A Ca-Al-rich inclusions in the Ningqiang carbonaceous chondrite: Evidence for partial melting in the nebula. Meteoritics and Planetary Science, 38, 407–417.

Lodders, K. (2003) Solar system abundances and condensation temperatures of the elements. The Astrophysical Journal, 591, 1220.

Loehman, R.E., Rao, C.N.R., and Honig, J.M. (1969) Crystallography and defect chemistry of solid solutions of vanadium and titanium oxides. Journal of Physical Chemistry, 73, 1781–1784.

Lord, H.C. (1965) Molecular equilibria and condensation in a solar nebula and cool stellar atmospheres. Icarus, 4, 279–288.

MacPherson, G.J. (2014) Calcium–Aluminum-Rich Inclusions in Chondritic Meteorites. In Treatise on Geochemistry Vol. 1, pp. 139–179. Elsevier.

MacPherson, G.J., and Grossman, L. (1984) “Fluffy” Type A Ca-, Al-rich inclusions in the Allende meteorite. Geochimica et Cosmochimica Acta, 48, 29–46.

Moore, P.B., Sen Gupta, P.K.., and Le Page, Y. (1989) Magnetoplumbite, Pb2+ Fe3+12O19: Refinement and Long-Pair Splitting. American Mineralogist, 74, 1186–1194.

Muller, D.A., Fitting Kourkoutis, L., Murfitt, M., Song, J.H., Hwang, H.Y., Silcox, J., Dellby, N., and Krivanek, O.L. (2008) Atomic-scale chemical imaging of composition and bonding by aberration-corrected microscopy. Science, 319, 1073–1076.

Nagashima, M., Armbruster, T., and Hainschwang, T. (2010) A temperature-dependent structure study of gem-quality hibonite from Myanmar. Mineralogical Magazine, 74, 871–885.

Newnham, E.E., and Haan, Y.M. DE (2014) Refinement of the a Al2O3, Ti2O3, V2O3 and Cr2O3 structures. Zeitschrift für Kristallographie - Crystalline Materials, 117, 235–237.

Okhotnikov, K., Charpentier, T., and Cadars, S. (2016) Supercell program: A combinatorial structure-generation approach for the local-level modeling of atomic substitutions and partial occupancies in crystals. Journal of Cheminformatics, 8, 17.

Onoda, M. (1998) Phase Transitions of Ti3O5. Journal of Solid State Chemistry, 136, 67–73.

Paque, J.M., Paque, and M., J. (1987) CaAl4O7 From Allende Type A Inclusion NMNH 4691. LPI, 18, 762.

Perdew, J.P., Burke, K., and Ernzerhof, M. (1996) Generalized gradient approximation made simple. Physical Review Letters, 77, 3865–3868.

Rakotondrazafy, M.A.F., Moine, B., and Cuney, M. (1996) Mode of formation of hibonite (CaAl12O19) within the U-Th skarns from the granulites of S-E Madagascar. Contributions to Mineralogy and Petrology, 123, 190–201.

Ramprasad, T., Mane, P., and Zega, T.J. (2018) Transmission Electron Microscope Analysis of a Spinel-Perovskite Assemblage Within a Refractory Inclusion from the Northwest Africa (NWA) 5028 CR2 Chondrite. In Lunar and Planetary Science Conference p. No. 2083.

Sapah, M.S. (2015) Characterization and chronology of refractory inclusions (CAIs) in the CV3 chondrite NWA 4502.

Schaffer, M., Schaffer, B., and Ramasse, Q. (2012) Sample preparation for atomic-resolution STEM at low voltages by FIB. Ultramicroscopy, 114, 62–71.

Scott, E.R.D., and Krot, A.N. (2014) Treatise on Geochemistry, ed. AM Davis. Oxford: Elsevier.

Shao, Y., Maunders, C., Rossouw, D., Kolodiazhnyi, T., and Botton, G.A. (2010) Quantification of the Ti oxidation state in BaTi1-xNbxO3 compounds. Ultramicroscopy, 110, 1014–1019.

Simon, Sutton, S.R., and Grossman (2009) First Ti-XANES analyses of refractory inclusions from Murchison. Lpsc, 60637, 1–2.

Simon, S.B., Grossman, L., and Davis, A.M. (1991) Fassaite composition trends during crystallization of

1156 Allende Type B refractory inclusion melts. Geochimica et Cosmochimica Acta, 55, 2635–2655.

1157 Simon S. B., Grossman L. and Davis A. M. (1997) Multiple generations of hibonite in spinel-hibonite

1158 inclusions from Murchison. Meteorit. Planet. Sci. 32, 259–269.

1159 Simon, S.B., Davis, A.M., and Grossman, L. (1999) Origin of compact type A refractory inclusions from

1160 CV3 carbonaceous chondrites. Geochimica et Cosmochimica Acta, 63, 1233–1248.

1161 Simon, S.B., Grossman, L., Hutcheon, I.D., Phinney, D.L., Weber, P.K., and Fallon, S.J. (2006) Formation

1162 of spinel-, hibonite-rich inclusions found in CM2 carbonaceous chondrites. American

1163 Mineralogist, 91, 1675–1687.

1164 Simon, S.B., Krot, A.N., Nagashima, K., Kööp, L., and Davis, A.M. (2019) Condensate refractory

1165 inclusions from the CO3.00 chondrite Dominion Range 08006: Petrography, mineral chemistry,

1166 and isotopic compositions. Geochimica et Cosmochimica Acta, 246, 109–122.

1167 Smyth, J.R., Swope, R.J., and Pawley, A.R. (1995) H in rutile-type compounds: II. Crystal chemistry of Al

1168 substitution in H-bearing stishovite. American Mineralogist, 80, 454–456.

1169 Srinivasan, G., Huss, G.R., and Wasserburg, G.J. (2000) A petrographic, chemical, and isotopic study of

1170 calcium-aluminum-rich inclusions and aluminum-rich chondrules from the Axtell (CV3) chondrite.

1171 Meteoritics and Planetary Science, 35, 1333–1354.

1172 Stoyanov, E., Langenhorst, F., and Steinle-Neumann, G. (2007) The effect of valence state and site

1173 geometry on Ti L3,2 and O K electron energy-loss spectra of TixOy phases. American

1174 Mineralogist, 92, 577–586.

1175 Tan, H., Turner, S., Yücelen, E., Verbeeck, J., and Van Tendeloo, G. (2011) 2D Atomic Mapping of

1176 Oxidation States in Transition Metal Oxides by Scanning Transmission Electron Microscopy and

1177 Electron Energy-Loss Spectroscopy.

1178 Tan, H., Verbeeck, J., Abakumov, A., and Van Tendeloo, G. (2012) Oxidation state and chemical shift

1179 investigation in transition metal oxides by EELS. Ultramicroscopy.

1180 Urban, K., Kabius, B., Haider, M., and Rose, H. (1999) A way to higher resolution: spherical-aberration
1181 correction in a 200 kV transmission electron microscope, 821–826 p. Journal of Electron
1182 Microscopy Vol. 48.
1183 Van Aken, P.A., and Liebscher, B. (2002) Quantification of ferrous/ferric ratios in minerals: New
1184 evaluation schemes of Fe L23 electron energy-loss near-edge spectra. Physics and Chemistry of
1185 Minerals, 29, 188–200.
1186 Van Aken, P.A., Liebscher, B., and Styrsa, V.J. (1998) Quantitative determination of iron oxidation
1187 states in minerals using Fe L2,3-edge electron energy-loss near-edge structure spectroscopy.
1188 Physics and Chemistry of Minerals, 25, 323–327.
1189 Weber, D., and Bischoff, A. (1997) Refractory inclusions in the CR chondrite Acfer 059 El Djouf 001:
1190 Petrology, chemical composition, and relationship to inclusion populations in other types of
1191 carbonaceous chondrites. CHEMIE DER ERDE-GEOCHEMISTRY, 57, 1–24.
1192 Wechsler, B.A., and Prewitt, C.T. (1984) Crystal structure of ilmenite (FeTiO3) at high temperature and
1193 at high pressure. American Mineralogist, 69, 176–185.
1194 Yamanaka, T., Hirai, N., and Komatsu, Y. (2002) Structure change of Ca1-xSrx TiO3 perovskite with
1195 composition and pressure. American Mineralogist, 87, 1183–1189.
1196 Yoneda, S., and Grossman, L. (1995) Condensation of CaO–MgO–Al2O3–SiO2 liquids from cosmic
1197 gases. Geochimica et Cosmochimica Acta, 59, 3413–3444.
1198 Zanetta, P.-M.P.-M., Le Guillou, C., Leroux, H., Zanda, B., Hewins, R.H., Lewin, E., and Pont, S. (2019)
1199 Modal abundance, density and chemistry of micrometer-sized assemblages by advanced electron
1200 microscopy: Application to chondrites. Chemical Geology, 514, 27–41.
1201 Zega, T., Nittler, L.R., Stroud, R.M., Division, T., and Berkeley, L. (2012) Measurement of the oxidation
1202 state of Ti in solar and presolar hibonite. Lunar and Planetary Science 43rd, 9, 4–5.
1203 Zega, T.J., Garvie, L.A.J., and Buseck, P.R. (2003) Nanometer-scale measurements of iron oxidation

1204 states of cronstedtite from primitive meteorites. American Mineralogist, 88, 1169–1172.

1205 Zega, T.J., Nittler, L.R., Busemann, H., Hoppe, P., and Stroud, R.M. (2007) Coordinated isotopic and

1206 mineralogic analyses of planetary materials enabled by in situ lift-out with a focused ion beam

1207 scanning electron microscope. Meteoritics and Planetary Science, 42, 1373–1386.

1208 Zega, T.J., Haenecour, P., and Floss, C. (2020) An in situ investigation on the origins and processing of

1209 circumstellar oxide and silicate grains in carbonaceous chondrites. Meteoritics and Planetary

1210 Science, 55, 1207–1227.

1211 Zega, T.J., Manga, V.R., Ciesla, F., Muralidharan, K., Watanabe, K., and Inada, H. (2021) Atomic-scale

1212 Evidence for Open-system Thermodynamics in the Early Solar Nebula. The Planetary Science

1213 Journal, 2, 115.

1214

1215

1216

Standard	$Ti^{4+}/\Sigma Ti$ ratio	Space group	Ti Symmetry	RMT Ti a.u.	RMT O a.u.	RKMax ($R_{mt} * K_{max}$)	Energy threshold (Ry)	Final Kmesh points	Final Kmesh point for supercell	Initial cif file
TiO_2	1	$P4_2/mnm$	D_{2h}	1.82	1.65	7	-6	2000	100	(Smyth et al. 1995)
$CaTiO_3$	1	Pmna	C_i	1.94	1.76	7	-6	200	10	(Yamanaka et al. 2002)
$FeTiO_3$	1	R-3C	C_{3i}	1.99	1.77	7	-7	500	10	(Wechsler and Prewitt 1984)
Ti_4O_7	0.7	P-1	C_1	1.74	1.57	7	-6	100	6	(Afir et al. 1999)
Ti_3O_5	0.5	C2/m	C_s	1.63	1.48	7	-6	100	5	(Onoda 1998)
Ti_2O_3	0	R3cH	C_{3i}	1.71	1.55	7	-6	100	10	(Newnham and Haan 2014)
TiO	(2+)	Fm-3m	O_h	1.96	1.77	7	-6	1000	100	(Loehman et al. 1969)
Hibonite	0.5 - 1	$P6_3/mmc$	C_{3v} and D_{3h}	1.74	1.63	7	-8	10	3	(Moore et al. 1989; Doyle et al. 2014)

Table 1: DOS parameters for the SCF calculations and optimization of the different species. Space group shown in Hermann-Mauguin notation; Ti symmetry shown in Schoenflies notation. RMT: muffin-tin radius, corresponding to the non-overlapping largest-atomic spheres in a spherically symmetric potential approximation. Ry; 1 Ry ≈ 13.605 eV. Kmesh point = sampling points in the irreducible wedge of the first Brillouin zone of the material. See text for more details. Visualization of the structures is presented in Fig. S2

Elements	*Wt%*	*At%*	*1 σ*	*pfu*
Mg	2.44	2.12	0.07	0.68
Si	0.16	0.12	0.02	0.04
Al	41.95	32.79	0.59	10.49
Cr	0.04	0.02	0.01	0.01
Ca	5.98	3.14	0.10	1.00
Fe	0.10	0.04	0.05	0.01
Ti	4.99	2.20	0.08	0.70
K	0.01	0.00	0.01	0.00
Mn	0.00	0.00	0.00	0.00
V	0.38	0.16	0.06	0.05
Na	0.00	0.01	0.02	0.00
P	0.01	0.00	0.02	0.00
Cl	0.00	0.00	0.00	0.00
O	45.06	59.40		19.00
Total	101.11	100.00	Sum cations	12.99

Table 2: Composition of the hibonite grain as measured via EPMA before FIB sampling. Composition given in weight percent (Wt%) and atomic percent (at%) and in cation per formula unit (pfu) based on 19 O atoms.

Figure 1: Stack of ELNES spectra of the Ti-bearing oxides. Two sets of data were processed and averaged for each sample. Spectra are ordered according to their $Ti^{4+}/\Sigma Ti$ ratio. White line integration windows defined by Stoyanov et al, (2007) are indicated in red (i.e. L_3 and L_2 windows). The boundaries of the single integration window for the edge onset method presented in this work are indicated in blue. See text for discussion of window width and placement. Peak positions are given in Table S2.

Figure 2: ELNES spectra of the synthetic (ALL series) stacked in order of increasing $Ti^{4+}/\Sigma Ti$ ratio and natural (NWA 5028) hibonite. Two sets of data were processed and averaged for each sample. White line integration windows defined by Stoyanov et al. (2007) are indicated in red (i.e. L_3 and L_2 windows). The single integration window for the edge onset method presented in this work is indicated in blue. Peak positions are given in Table S3.

Figure 3: The white-line ratio shown as a function of Ti oxidation state. a) Application of the white-line ratio method using the window positions and the background subtraction method detailed in Stoyanov et al, (2007). Both Ti-bearing oxides (blue crosses) and synthetic hibonites (red circles) are plotted. The fitted curve formula is given in the top left corner of the graphic. b) The L_2 edge intensity (after normalization; see text for details) plotted as a function of $Ti^{4+}/\Sigma Ti$. Both Ti-bearing oxides (blue crosses) and synthetic hibonites (red circles) are plotted. Large variations are revealed for samples with similar $Ti^{4+}/\Sigma Ti$ close to 1 (i.e., $CaTiO_3$, TiO_2, $FeTiO_3$ and synthetic hibonites).

Figure 4: ELNES from experimental (dashed curves) measurements and DFT calculations (solid curves). a) TELNES (DOS + Broadening) calculation of the previously listed Ti-bearing oxide standards compared to their experimental spectra. b) TELNES (DOS + Broadening) calculation of two hibonite structures with distinct Ti oxidation states (as indicated, $\%Ti^{4+}$=0.5-1) compared to the synthetic hibonite experimental spectra. All spectra are normalized to their maxima. In the $\%Ti^{4+}$= 1 case, Ti substitutes on the M4 site; in the $\%Ti^{4+}$=0.5 case, Ti is distributed over the M2 and M4 sites.

Figure 5: The normalized L_3 intensity, single window, as shown in Figs. 1 and 2, as a function of the Ti^{4+} concentration*. Synthetic hibonite with known Ti^{4+}/Ti^{3+} falls on the same correlation line. Blue crosses are Ti-bearing oxide standards. Red circles are the synthetic hibonite samples from Beckett et al. (1988). The red line corresponds to the quadratic expression fit to the data (equation shown at top). Dashed black curves represents the error dispersion. This correlation enables determination of the $Ti^{4+}/\Sigma Ti$ ratio (0.86±0.01) of the hibonite grain sampled in NWA 5028 (green lines). The green area represents the error on the determination of the oxidation state.*

Figure 6. Microprobe data on a CTA CAI from the NWA 5028 CR2 chondrite. a) Backscattered electron (BSE) image of the CTA CAI showing where the hibonite grain was extracted (orange rectangle). The region of interest is located at the edge of a dark (in BSE contrast) rim that surrounds the CTA (e.g, Ramprasad et al., 2018). b) BSE image of the RS2 area (e.g, Ramprasad et al., 2018) showing the hibonite grain (indicated by orange arrow and outlined with a white dotted curve). c) Higher magnification BSE image of the hibonite grain. The grain exhibits sharp boundaries indicated by a dashed white curve. Surrounding phases are identified. The orange rectangle represents the location of the FIB transect.

Figure 7: Aberration-corrected STEM and diffraction data on hibonite extracted from NWA 5028. a) Low magnification HAADF - STEM image showing hibonite grains and adjacent perovskite. Some curtaining appears (relatively dark vertical lines) as a result of ion milling of material with different sputtering rates. Areas from which diffraction and image data were acquired are indicated. b) Higher magnification HAADF – STEM image revealing lattice fringes of the oriented hibonite. c) SAED pattern of hibonite from NWA 5028, viewed down the $[11\bar{2}0]$ zone axis. Measurement of the pattern along the vertical direction reveals an interplanar spacing of 2.2 nm consistent with the c-axis of hibonite.

Figure 8: Quantified element maps acquired by TEM-EDS and presented in cation pfu (160×160 pixels). This dataset was acquired from the region shown in Figure 7a. Only major elements are plotted.

Figure 9: Quantification of the STEM-EDS data for hibonite grain 1 (hib.1 - see Fig.7a). Composition shown per formula unit assuming Al+Ca+Mg+Ti+Si+Fe+V+Cr=13. Each point represents a quantified pixel of the rebinned EDS map (10×10 pixels).

Figure 10: STEM-EELS data on hibonite grain 1. a) A map (40×40 pixels) of the $Ti^{4+}/\Sigma Ti$ ratio (hib.1 - see Fig.7a) determined using EELS by the edge-onset method. $Ti^{4+}/\Sigma Ti$ decreases from the interior (higher in the panel) to the grain boundary at the bottom. b) The chemical shift of the Ti $L_{2,3}$ edge (before double-step function removal) visible between the boundary of the grain (bottom part of the image) and the core.

Figure 11: Experimental and simulated STEM-HAADF images of hibonite. a) Atomic-resolution STEM-HAADF data from hibonite grain boundary (see Figure 7a). b) HAADF image showing the location of atomic-scale measurements (Fig. 12). Atomic columns are visible in this $[11\bar{2}0]$ projection. The map is acquired near the grain boundary. c) High-contrast HAADF image showing the presence of brighter spots on the face sharing M4 sites and weak contrast on the M3 site (white ellipses). d) image simulation (QSTEM®) of a nominal hibonite compared to a model in the same orientation $[11\bar{2}0]$. The ball-and-stick model shows 1:1 correspondence with the atomic position visible on the experimental HAADF image and in the simulation. Each site is indicated as a color, e.g., Ca (red), O (black) and the Al sites which are listed from M1 to M5. e) Image simulation with aberrations of a nominal hibonite. f) Image simulation of hibonite containing 0.7 pfu of Ti and Mg substituting on M4 site and M3 site respectively. A model in the same orientation is compared. The white ellipses circle the site of Ti substitution (M4) g) Image simulation of the same hibonite (0.7 pfu of Ti/Mg) with aberrations. The white ellipses show the replica of the brighter spot. The space between the blocks are darker than in e) due to the lower Z value as a result of Mg substituting into the M3 site.

Figure 12: Atomic-resolution EELS mapping of the local area shown by the orange box in Fig. 11b in the $[11\bar{2}0]$ orientation. (a) HAADF reference image. (b) Ca $L_{2,3}$ atomic-resolution EELS map. (c) Ti $L_{2,3}$ atomic-resolution EELS map. (d) $Ti^{4+}/\Sigma Ti$ map. Pixels containing low Ti $L_{2,3}$ intensity were masked to better reveal the relationship with the Ti columns and the $Ti^{4+}/\Sigma Ti$ ratio. The map exhibits variation of $Ti^{4+}/\Sigma Ti$ of 0.4 with an error of ±0.08.

Figure 13: Mg_{Excess} in cation per formula unit (Mg/Ti^{4+}) compared to the $Ti^{4+}/\Sigma Ti$ ratio determined by our single window approach in a hibonite grain of NWA5028. The superimposed orange arrows in the plot correspond to reaction 4 (vertical arrow) and to the reaction 7 (diagonal arrow). The vertical only impacts the Mg concentration, whereas the diagonal line corresponds to Ti^{3+} replacing Ti^{4+} and increasing the isolated Mg defect. The horizontal dashed line corresponds to Mg=Ti or an ideal 1:1 correlation between Mg^{2+} and Ti^{4+}. Error bars are plotted according to the EDS quantification accuracy and the error discussed in section 4.2.

Figure 14: Schematic of the formation and evolution of the hibonite grain selected near the rim of the CTA CAI. Two pathways 1 and 2 are considered, with each consisting of formation and equilibration stages 1 and 2, respectively in the solar protoplanetary disk. See the text for discussion. Ultimately, the grain did not reach equilibrium and contains an element and Ti-oxidation-state gradient. The direction of the $Ti^{4+}/\Sigma Ti$ gradient is different from the direction of the elemental gradient (orange arrows vs white/blue or white/green arrows in the bottom row).

Figure 1

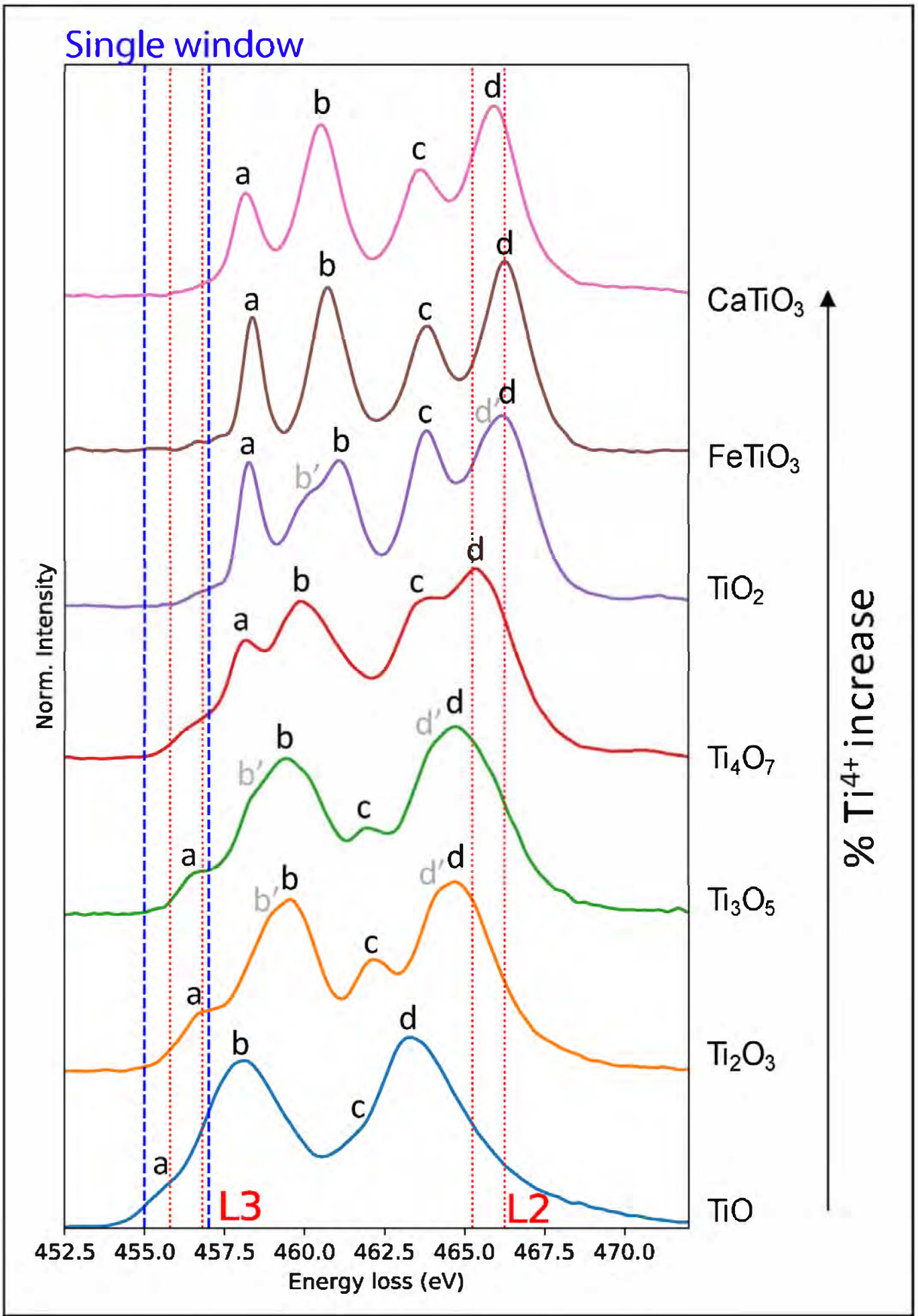
Single window
a
b
c
d
b′
d′
CaTiO3
FeTiO3
TiO2
Ti4O7
Ti3O5
Ti2O3
TiO
L3
L2
Norm. Intensity
452.5
455.0
457.5
460.0
462.5
465.0
467.5
470.0
Energy loss (eV)
% Ti4+ increase

Figure 2

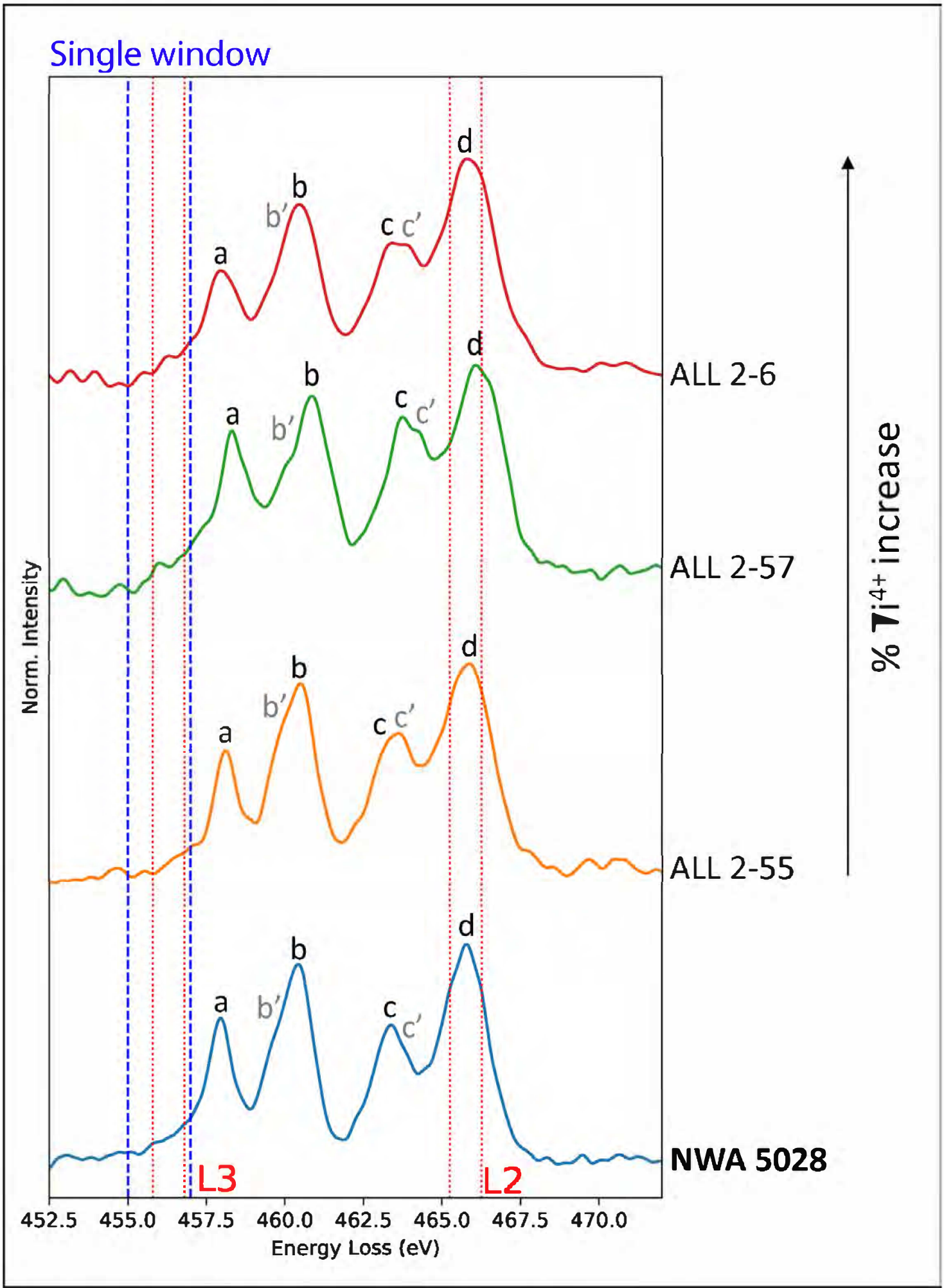
Single window
a
b′
b
c c′
d
ALL 2-6
ALL 2-57
ALL 2-55
NWA 5028
Norm. Intensity
% Ti4+ increase
L3
L2
452.5 455.0 457.5 460.0 462.5 465.0 467.5 470.0
Energy Loss (eV)

Figure 3

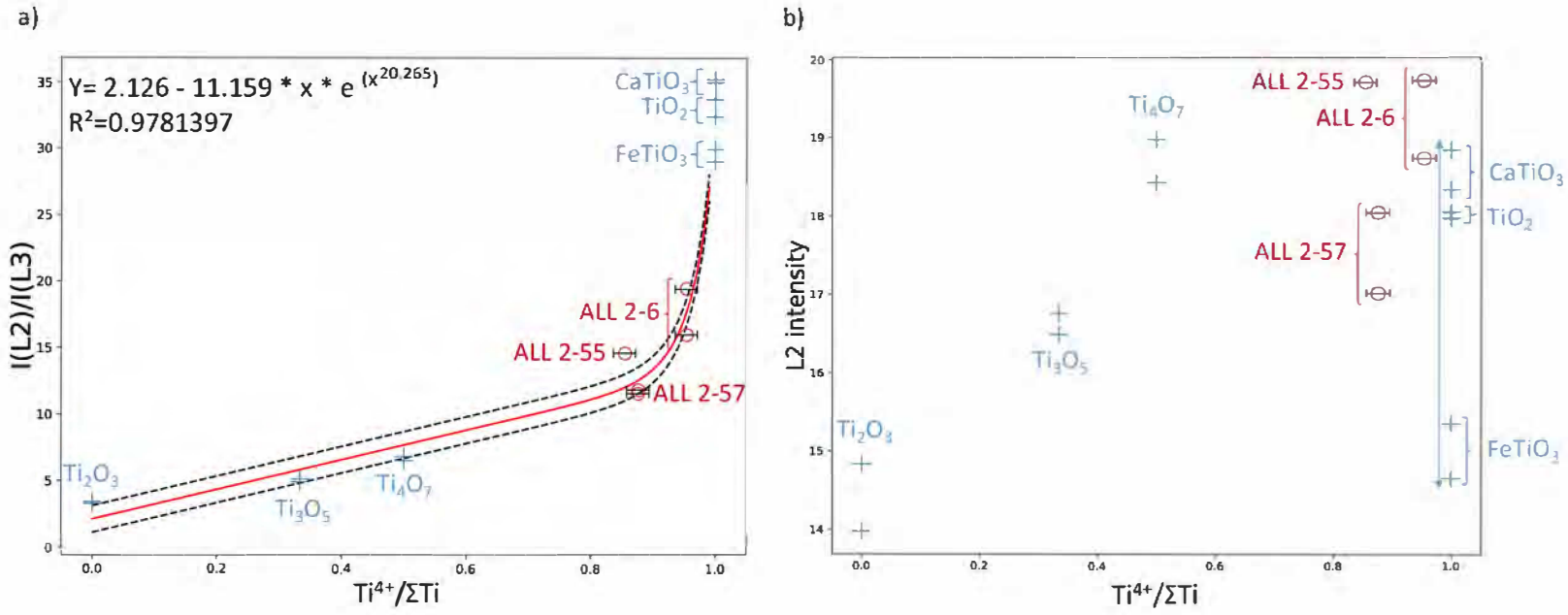
a)
Y= 2.126 - 11.159 * x * e (x^20.265)
R²=0.9781397
CaTiO3
TiO2
FeTiO3
ALL 2-6
ALL 2-55
ALL 2-57
Ti2O3
Ti3O5
Ti4O7
I(L2)/I(L3)
Ti4+/ΣTi
b)
ALL 2-55
ALL 2-6
ALL 2-57
Ti4O7
Ti3O5
Ti2O3
CaTiO3
TiO2
FeTiO3
L2 intensity
Ti4+/ΣTi

Figure 4

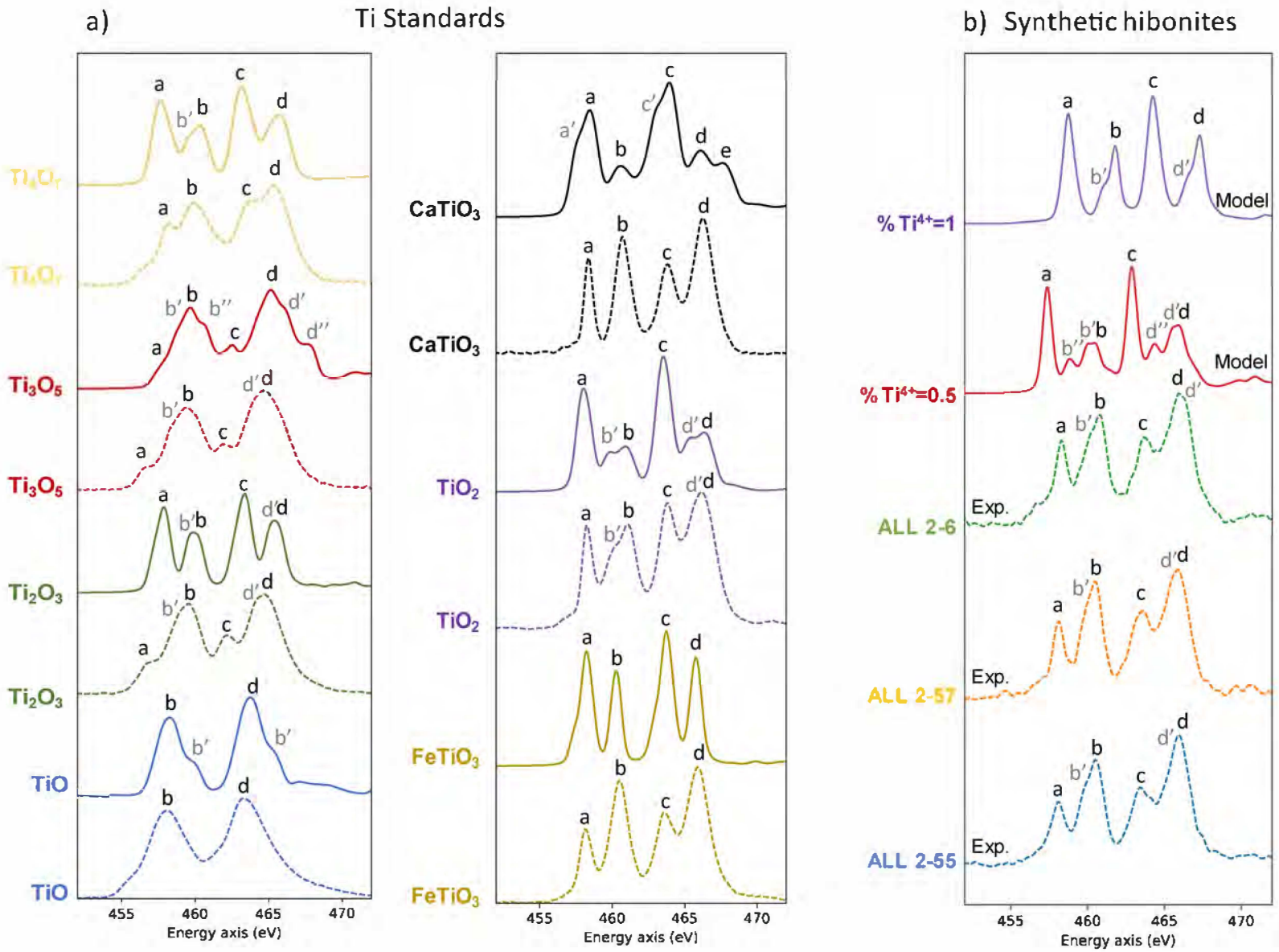
a)
Ti Standards
b) Synthetic hibonites
Ti_4O_7
Ti_4O_7
Ti_3O_5
Ti_3O_5
Ti_2O_3
Ti_2O_3
TiO
TiO
$CaTiO_3$
$CaTiO_3$
TiO_2
TiO_2
$FeTiO_3$
$FeTiO_3$
% Ti^{4+}=1
% Ti^{4+}=0.5
ALL 2-6
ALL 2-57
ALL 2-55
Model
Model
Exp.
Exp.
Exp.
455
460
465
470
Energy axis (eV)
Energy axis (eV)
Energy axis (eV)

Figure 5

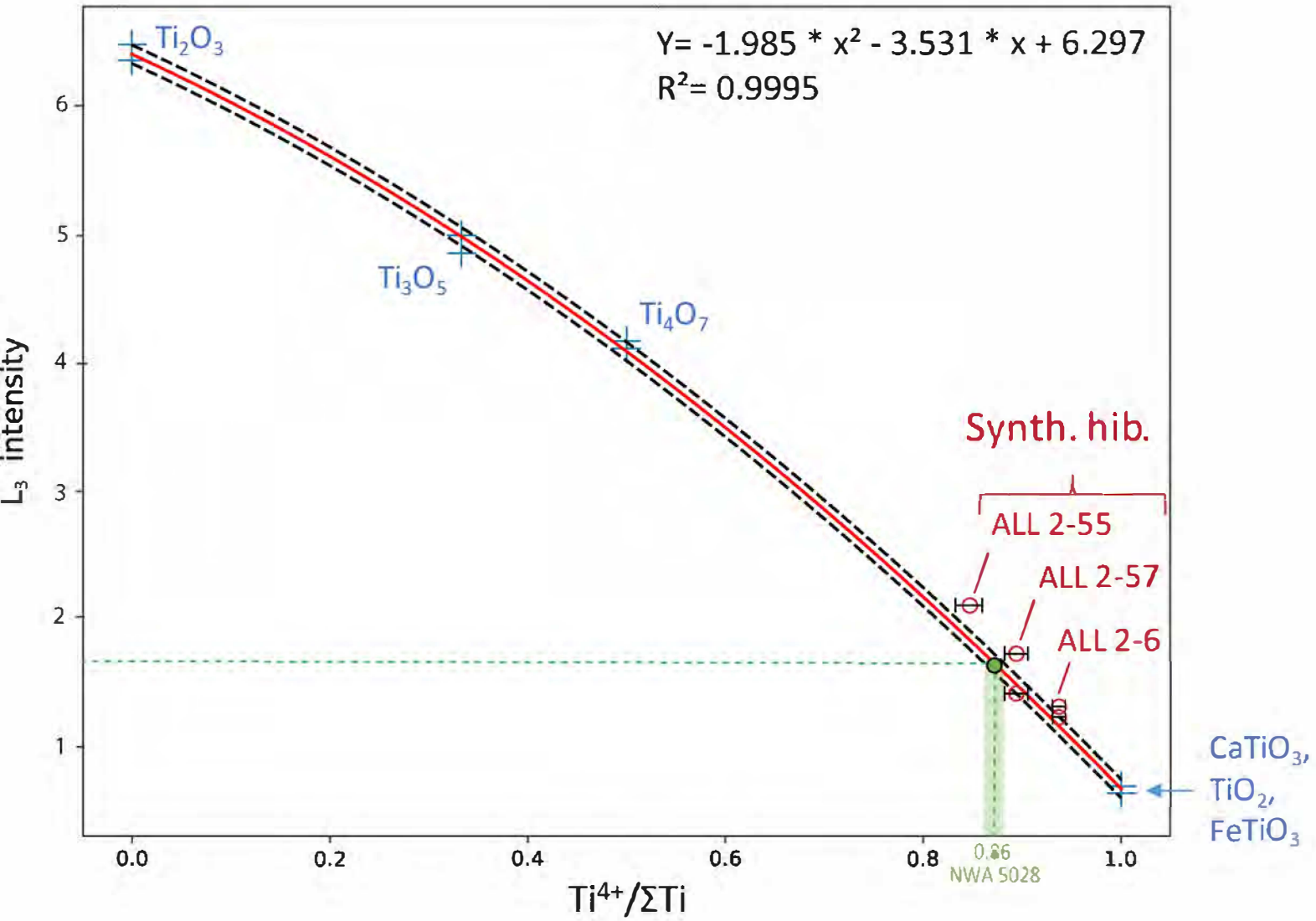
Y= -1.985 * x² - 3.531 * x + 6.297
R²= 0.9995
Ti2O3
Ti3O5
Ti4O7
Synth. hib.
ALL 2-55
ALL 2-57
ALL 2-6
CaTiO3,
TiO2,
FeTiO3
0.86
NWA 5028
L3 intensity
Ti4+/ΣTi
0.0
0.2
0.4
0.6
0.8
1.0
1
2
3
4
5
6

Figure 6

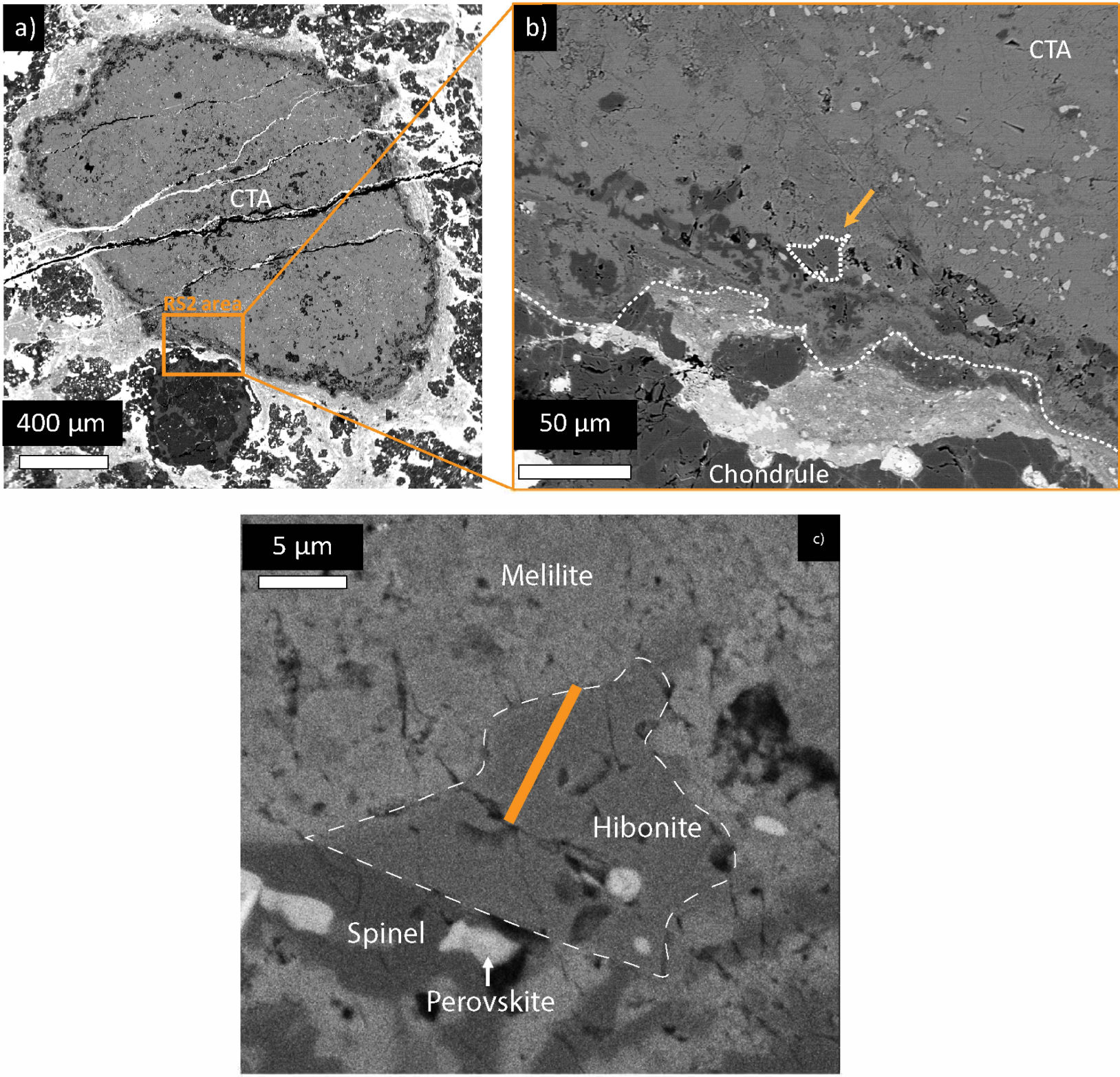
a)
CTA
RS2 area
400 µm
b)
CTA
50 µm
Chondrule
5 µm
c)
Melilite
Hibonite
Spinel
Perovskite

Figure 7

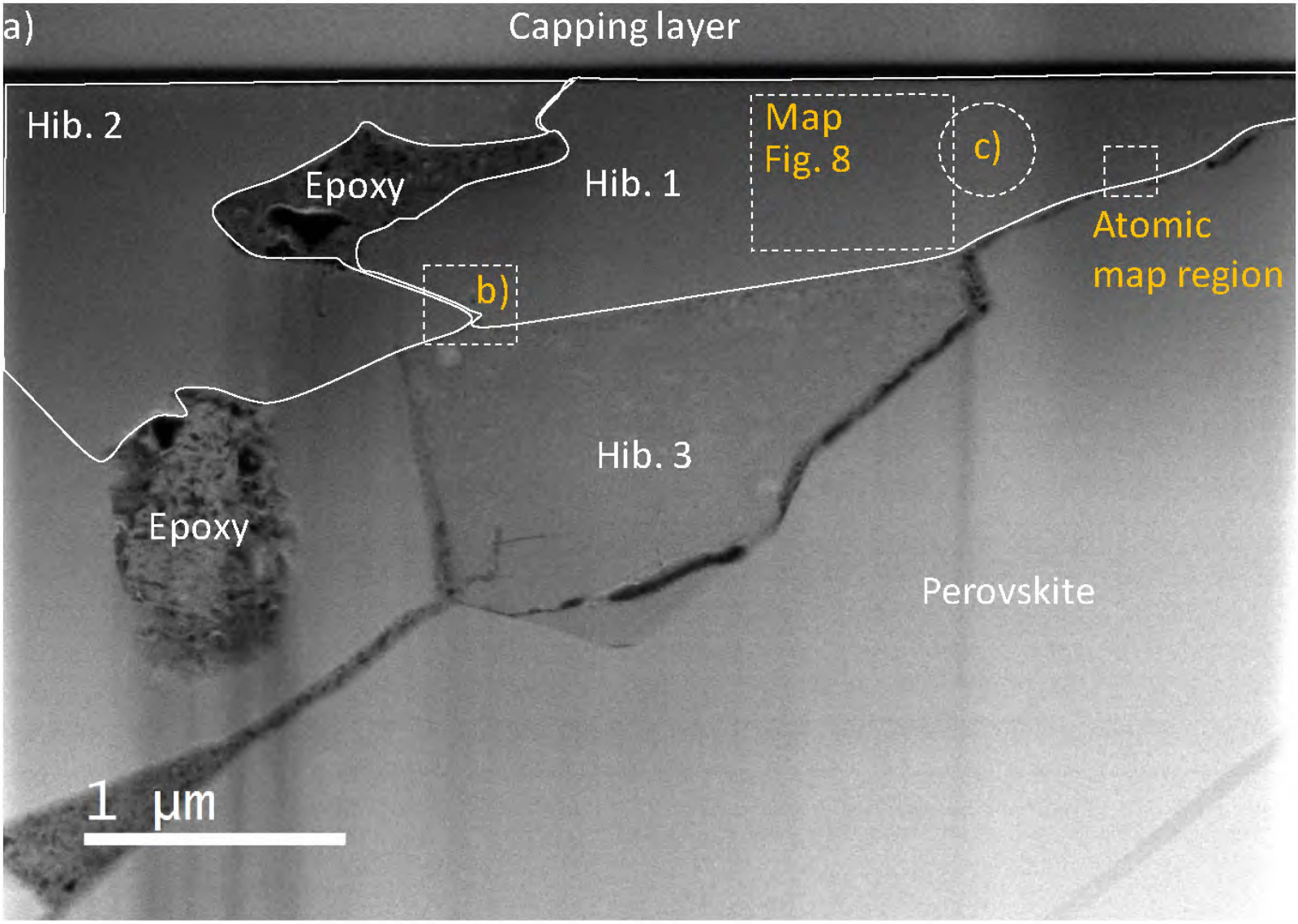
a)
Capping layer
Hib. 2
Epoxy
Hib. 1
Map
Fig. 8
c)
Atomic
map region
b)
Hib. 3
Epoxy
Perovskite
1 µm

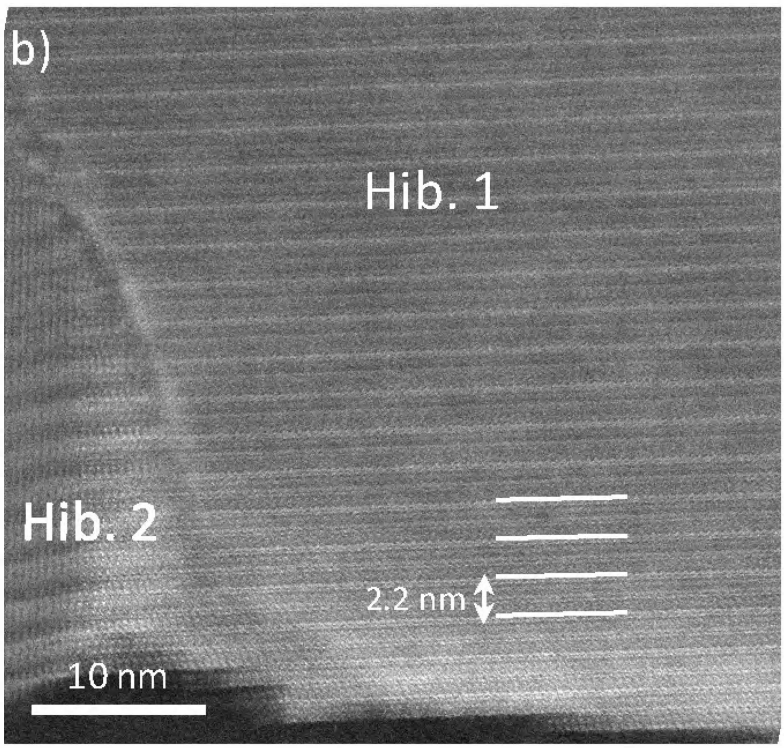
b)
Hib. 1
Hib. 2
2.2 nm
10 nm

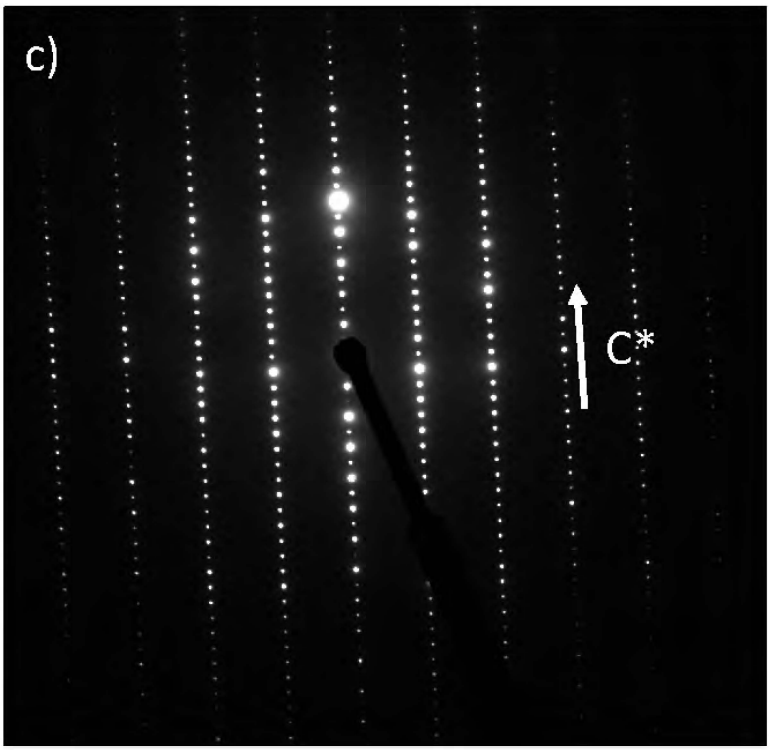
c)
C*

Figure 8

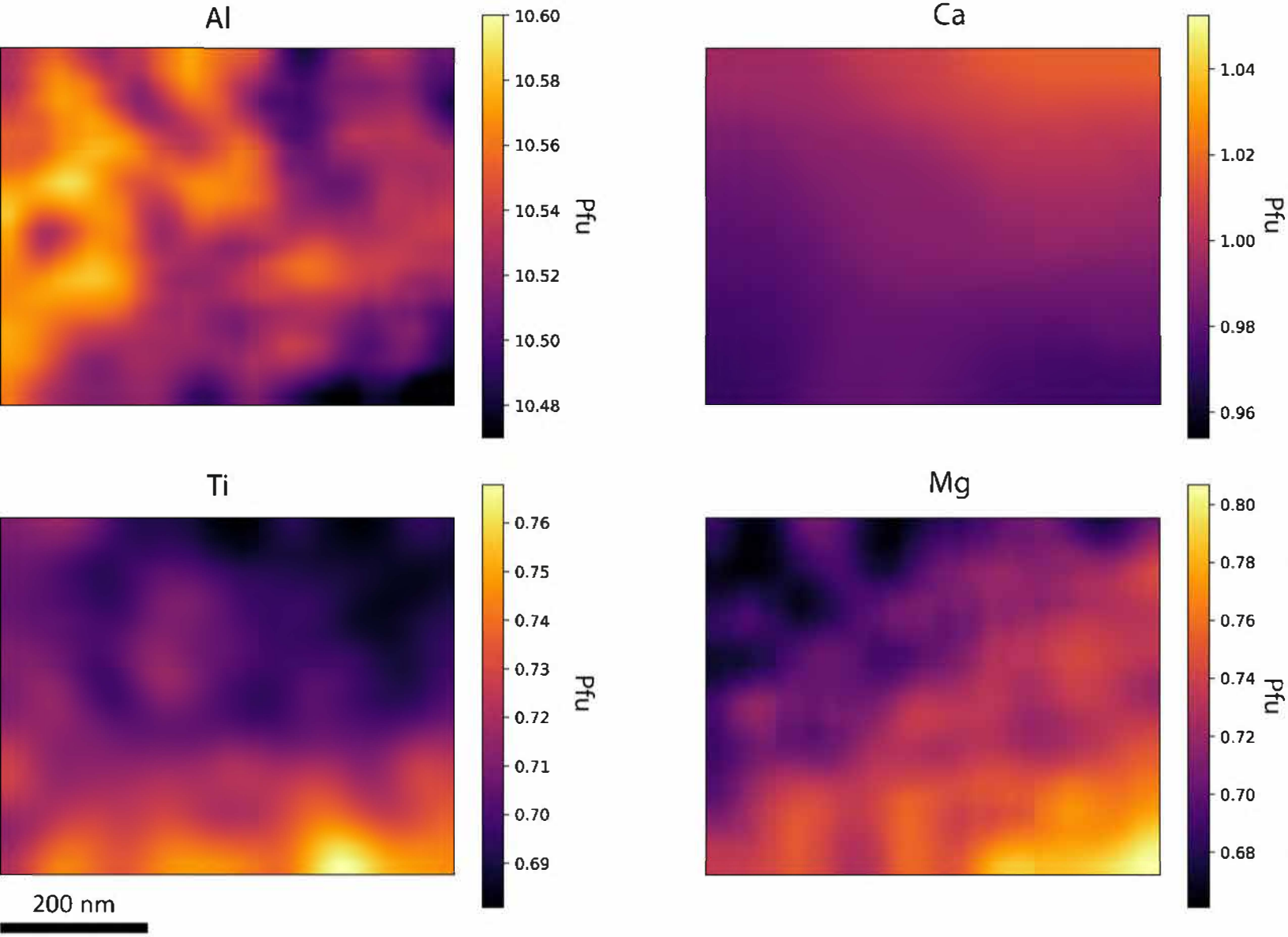
Al
10.60
10.58
10.56
10.54
10.52
10.50
10.48
Pfu
Ca
1.04
1.02
1.00
0.98
0.96
Pfu
Ti
0.76
0.75
0.74
0.73
0.72
0.71
0.70
0.69
Pfu
Mg
0.80
0.78
0.76
0.74
0.72
0.70
0.68
Pfu
200 nm

Figure 9

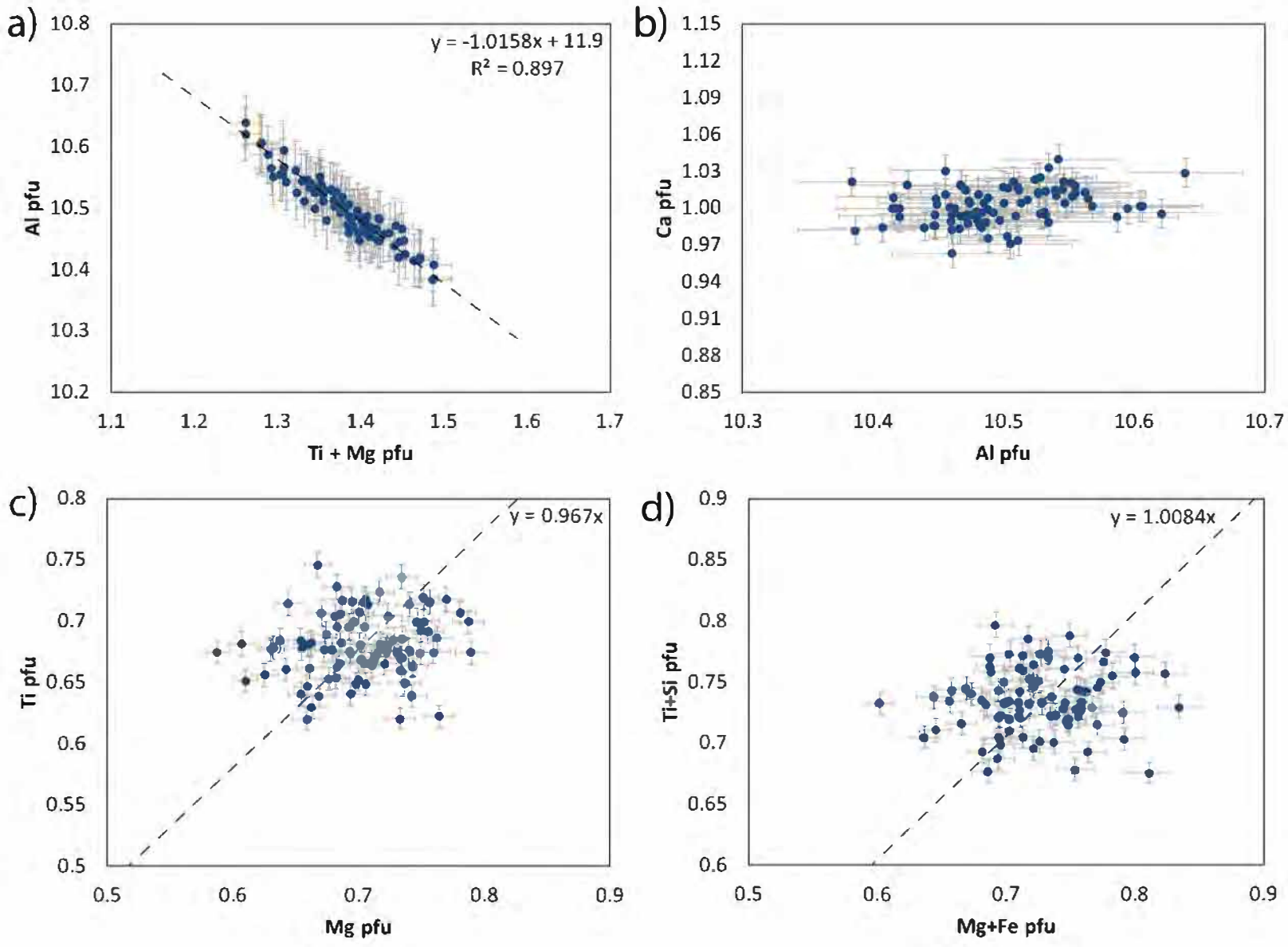
a)
y = -1.0158x + 11.9
R² = 0.897
Al pfu
Ti + Mg pfu
b)
Ca pfu
Al pfu
c)
y = 0.967x
Ti pfu
Mg pfu
d)
y = 1.0084x
Ti+Si pfu
Mg+Fe pfu

Figure 10

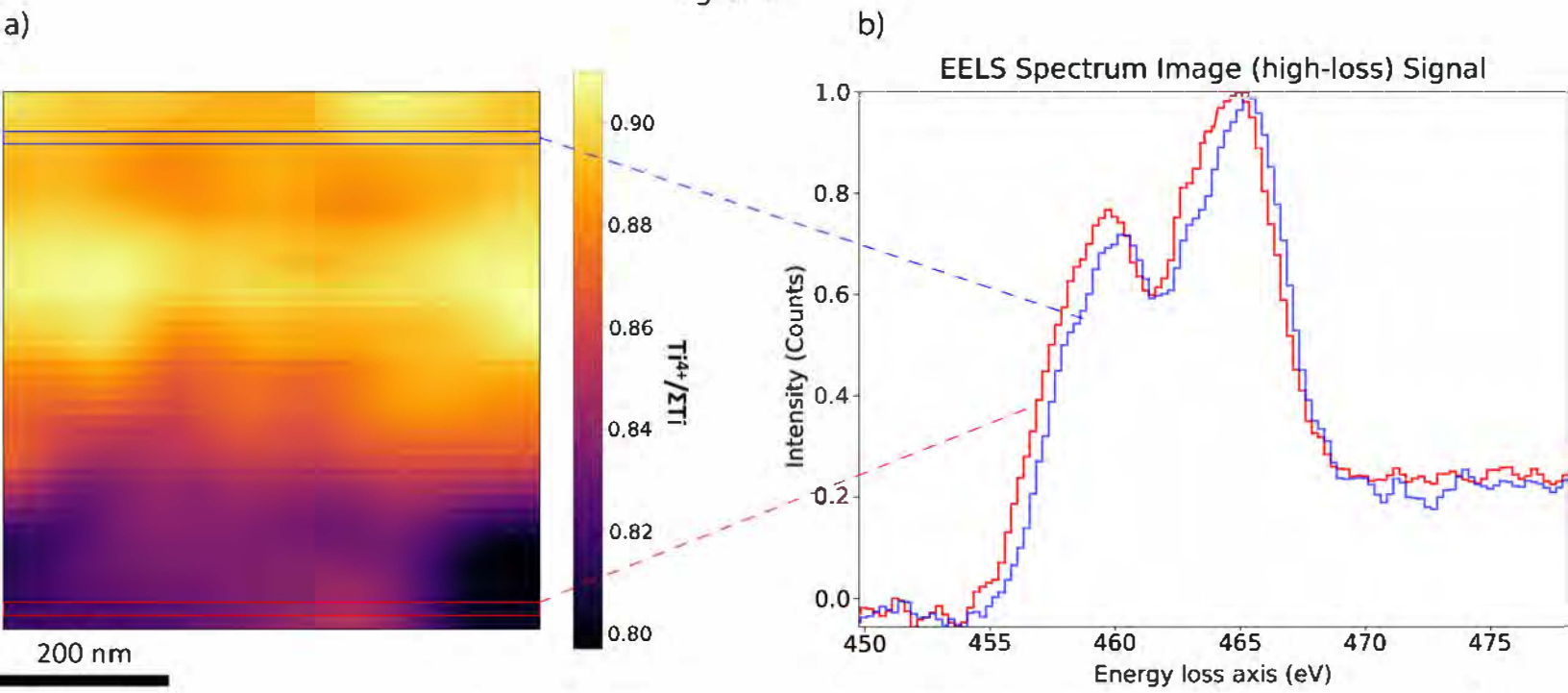
a)
b)
EELS Spectrum Image (high-loss) Signal
0.90
0.88
0.86
0.84
0.82
0.80
Ti4+/ΣTi
200 nm
1.0
0.8
0.6
0.4
0.2
0.0
Intensity (Counts)
450
455
460
465
470
475
Energy loss axis (eV)

Figure 11

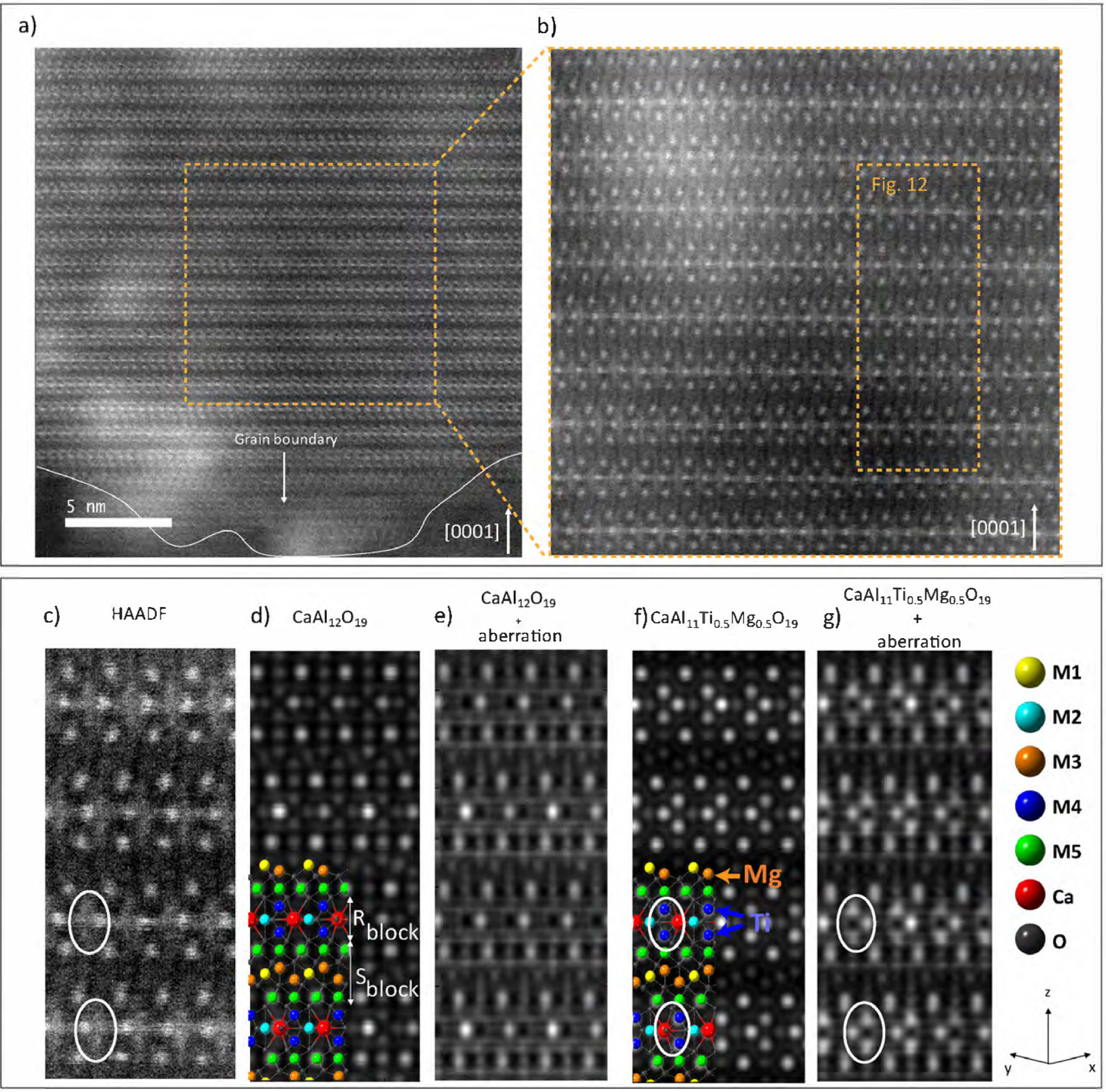
a)
b)
Grain boundary
5 nm
[0001]
Fig. 12
[0001]
c) HAADF
d) $CaAl_{12}O_{19}$
e) $CaAl_{12}O_{19}$ + aberration
f) $CaAl_{11}Ti_{0.5}Mg_{0.5}O_{19}$
g) $CaAl_{11}Ti_{0.5}Mg_{0.5}O_{19}$ + aberration
R_{block}
S_{block}
Mg
Ti
M1
M2
M3
M4
M5
Ca
O
z
y
x

Figure 12

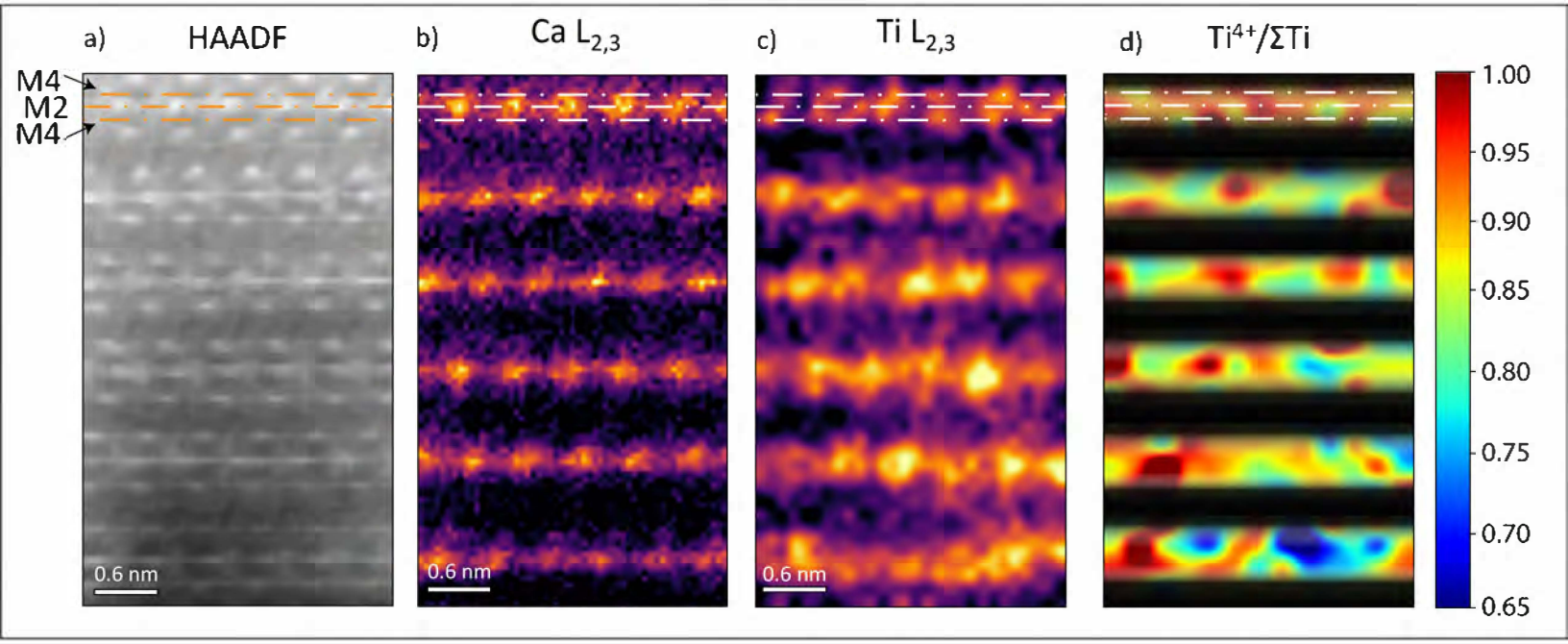
a)
HAADF
b)
Ca L2,3
c)
Ti L2,3
d)
Ti4+/ΣTi
M4
M2
M4
0.6 nm
0.6 nm
0.6 nm
1.00
0.95
0.90
0.85
0.80
0.75
0.70
0.65

Figure 13

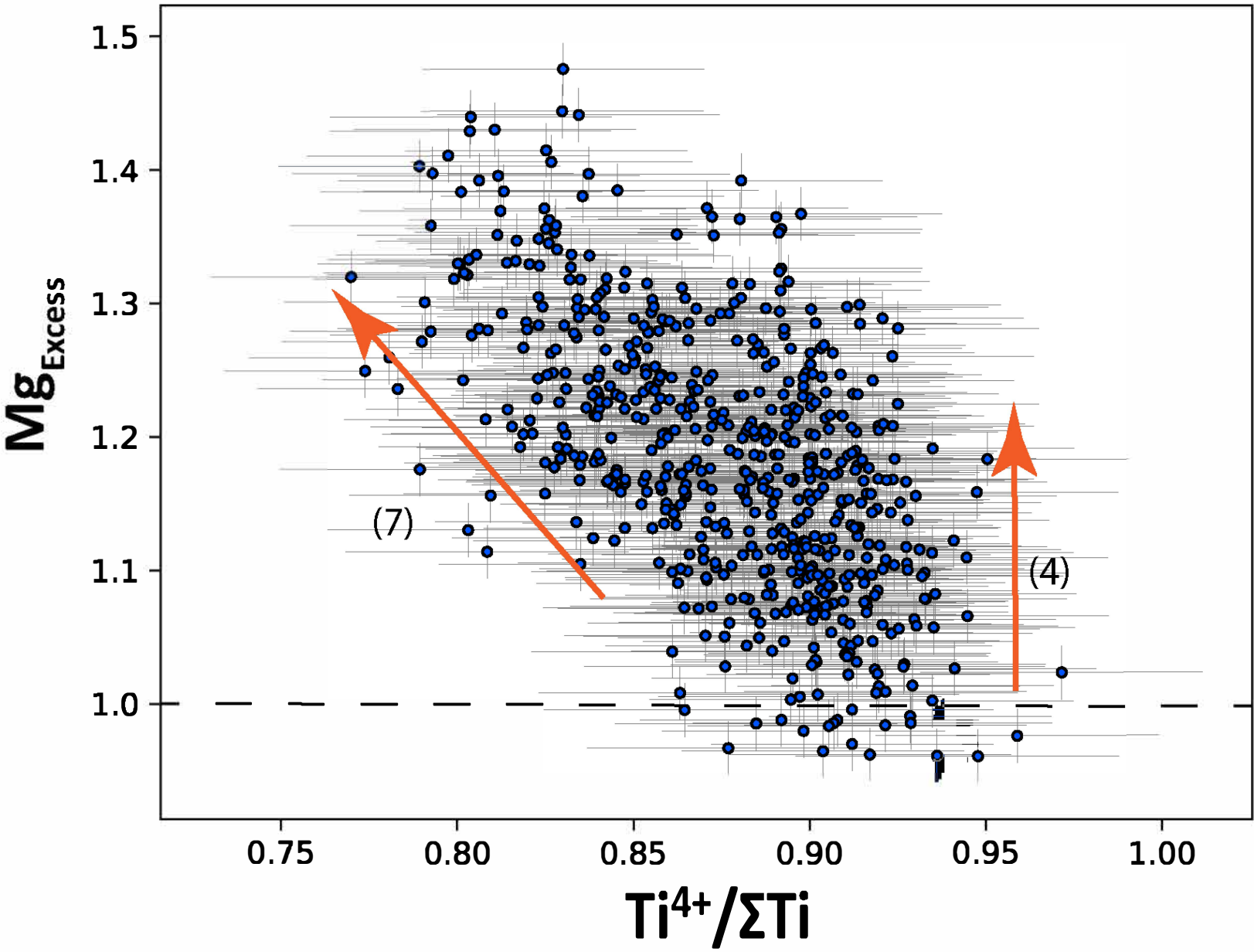

Figure 14

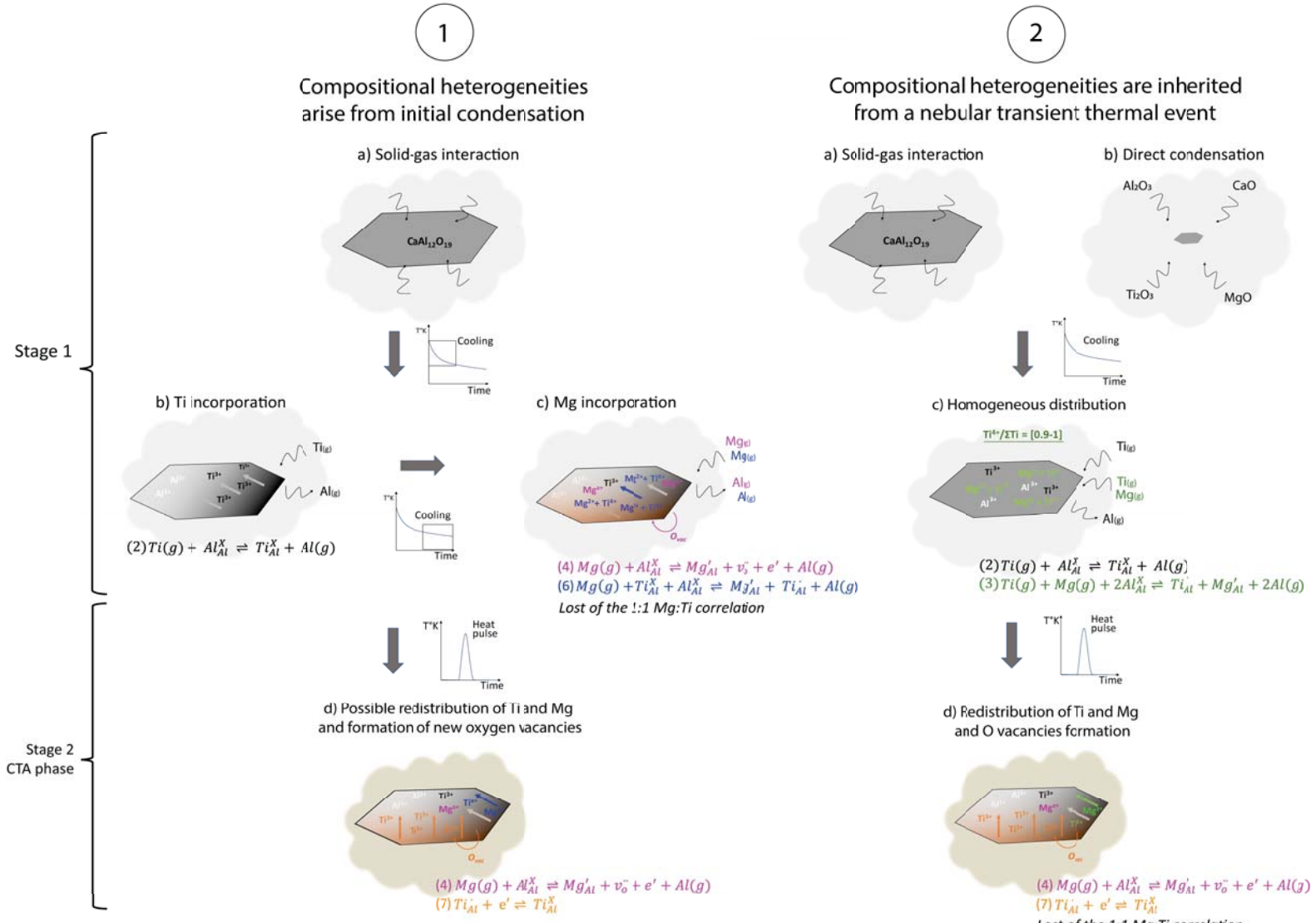
1
Compositional heterogeneities arise from initial condensation
2
Compositional heterogeneities are inherited from a nebular transient thermal event
Stage 1
Stage 2 CTA phase
a) Solid-gas interaction
b) Ti incorporation
c) Mg incorporation
d) Possible redistribution of Ti and Mg and formation of new oxygen vacancies
a) Solid-gas interaction
b) Direct condensation
c) Homogeneous distribution
d) Redistribution of Ti and Mg and O vacancies formation
Cooling
Heat pulse
Time
(2) $Ti(g) + Al_{Al}^{X} \rightleftharpoons Ti_{Al}^{X} + Al(g)$
(4) $Mg(g) + Al_{Al}^{X} \rightleftharpoons Mg'_{Al} + v_o^{\cdot\cdot} + e' + Al(g)$
(6) $Mg(g) + Ti_{Al}^{X} + Al_{Al}^{X} \rightleftharpoons Mg'_{Al} + Ti_{Al}^{\cdot} + Al(g)$
Lost of the 1:1 Mg:Ti correlation
(3) $Ti(g) + Mg(g) + 2Al_{Al}^{X} \rightleftharpoons Ti_{Al}^{\cdot} + Mg'_{Al} + 2Al(g)$
(7) $Ti_{Al}^{\cdot} + e' \rightleftharpoons Ti_{Al}^{X}$
Ti3+/ΣTi = [0.9-1]